

# A 3D-1D-0D Multiscale Model of the Neuro-Glial-Vascular Unit for Synaptic and Vascular Dynamics in the Dorsal Vagal Complex

Alexander Hermann<sup>\*1,2</sup>[0000-0002-9731-3286], Tobias Köpp<sup>3</sup>[0000-0003-3548-2807],  
 Andreas Wagner<sup>4</sup>[0000-0002-1622-846X], Arman Shojaei<sup>1</sup>[0000-0001-8638-8285],  
 Barbara Wohlmuth<sup>4</sup>[0000-0001-6908-6015], Roland Aydin<sup>1</sup>[0000-0002-9542-9146],  
 Christian J. Cyron<sup>1,5</sup>[0000-0002-0715-6484], and Roustem Miftahof<sup>5</sup>[0000-0001-8264-0885]

<sup>1</sup> Institute of Material Systems Modeling, Helmholtz-Zentrum Hereon, Max-Planck-Str. 1, 21502 Geesthacht, Germany

<sup>2</sup> CAU Innovation GmbH, Fraunhoferstraße 13, 24118 Kiel, Germany

<sup>3</sup> Fraunhofer-Institut FOKUS, Kaiserin-Augusta-Allee 31, 10589 Berlin, Germany

<sup>4</sup> Department of Mathematics, Technical University of Munich, Garching, Germany

<sup>5</sup> Institute for Continuum and Material Mechanics, Hamburg University of Technology, Eissendorfer Strasse 42, 21073 Hamburg, Germany

\* Corresponding author: alexander.hermann@hereon.de

**Abstract.** Cerebral blood flow regulation is critical for brain function, and its disruption is implicated in various neurological disorders. Many existing models do not fully capture the complex, multiscale interactions among neuronal activity, astrocytic signaling, and vascular dynamics—especially in key brainstem regions. In this work, we present a 3D-1D-0D multiscale computational framework for modeling the neuro-glial-vascular unit (NGVU) in the dorsal vagal complex (DVC). Our approach integrates a quadripartite synapse model—which represents the interplay among excitatory and inhibitory neurons, astrocytes, and vascular smooth muscle cells—with a hierarchical description of vascular dynamics that couples a three-dimensional microcirculatory network with a one-dimensional macrocirculatory representation and a zero-dimensional synaptic component. By linking neuronal spiking, astrocytic calcium and gliotransmitter signaling, and vascular tone regulation, our model reproduces key features of functional hyperemia and elucidates the feedback loops that help maintain cerebral blood flow. Simulation results demonstrate that neurotransmitter release triggers astrocytic responses that modulate vessel radius to optimize oxygen and nutrient delivery. This integrated framework, to our knowledge the first model to combine these elements for the NGVU in the DVC, provides a robust and modular platform for future investigations into the pathophysiology of cerebral blood flow regulation and its role in autonomic control, including the regulation of stomach function.

**Keywords:** Multiscale Modeling · Neuro-Glial-Vascular Unit · Dorsal Vagal Complex · Functional Hyperemia · Synaptic Dynamics · Vascular Tone Regulation

## 1 Introduction

Understanding perception, cognition, learning, memory and consciousness in the brain are the prime objectives of neuroscience. Until now, research on the brain has been dom-

inated by both experimental and theoretical reductionism, which emphasizes detailed knowledge of its structure and function at a high-resolution level. Successful examples of this approach include a computationally intensive reconstruction of morphological constituents in a cubic millimeter of the human temporal cortex at a nanometer scale [153]; the uncovering of cellular diversity at the transcriptomics level [150]; real-time monitoring of the dynamics of synaptic plasticity using genetically encoded, intensimetric fluorescence indicators [160]. Although purely reductive strategies provide amazing insights into the functional intricacies of biological matter, they unequivocally neglect the context in which these processes operate. This severely limits the ability of reductionism to explain how and why the brain behaves as it does. Notable examples of the conceptual and expensive shortcomings are The Blue Brain, The European Human Brain, and The Cajal Blue Brain Projects—research initiatives that intended but failed to create a digital replica of functional mouse and human brains. The reductive trend continues to prevail in *in vitro* and *in vivo* studies of brain function under physiological and disease states. It is attractive from experimental and theoretical perspectives to investigate a single target in isolation, such as dopamine neurotransmission in the pathogenesis of Parkinson’s disease, neuronal activity in the pathophysiology of epilepsy, or cerebral blood flow (CBF) in stroke and vascular dementia patients. However, being deterministic in nature, the underlying physiological processes run at multi-hierarchical levels and cannot be accounted for by reductionism. This shift has led to a change in the paradigm of studying the finely parcellated brain, moving from a reductionist approach to an integrative analysis at different levels of its organization.

The concept of the neurovascular unit (NVU) as a functional element of the brain was proposed and formalized in 2001 at the inaugural Stroke Progress Review Group meeting of the National Institute of Neurological Disorders and Stroke [85]. Initially, it was defined morphologically as a hetero-cellular structure composed of neurons, endothelial cells (ECs), vascular smooth muscle cells (SMCs), and the extracellular matrix. The NVU was assigned *a priori* properties of functional homogeneity and generality throughout the brain [150]. Over the years, the concept has evolved from its “canonical” form to a neuro-glial-vascular unit (NGVU), incorporating additional cellular constituents such as astrocytes and pericytes, to highlight the multi-functional, -dimensional, and -cellular coordinated function of the brain. Recent single-cell RNA-seq analyses have proven the molecular heterogeneity of brain cells [169]. This has inferred the functional diversity of NGVUs that depends on topological cell arrangements, regional specialization, and the metabolic demands of different brain areas. The most investigated function of the NVU is neurovascular coupling, i.e., the matching of blood flow to neuronal metabolic demands, also known as functional hyperemia. Although the large vessel architecture of the brain is established at birth, the intracerebral vascular network grows postnatally, known as capillary angiogenesis, to match cortical expansion [116]. Two main cell types, ECs and pericytes, embedded in the basal lamina, constitute the wall of capillaries. ECs linked via gap junctions create a smooth luminal syncytium of the capillaries. These are ensheathed externally by pericytes. These cells have variable morphology ranging from circumferential, longitudinal to amoeboid depending on the location along the vascular tree [76]. Pericytes mediate precise local changes of capillary diameter in response to excitatory/inhibitory signals arriving from

the neurons and astrocytes. Coupled via gap junctions, pericytes and ECs together sustain the conduction of locally induced signals along the capillary and arteriolar networks and thus regulate CBF over space and time [74, 109, 22, 145, 49, 50, 131, 86].

During capillary angiogenesis, astrocytes undergo massive proliferation. The basal lamina of blood vessels and the astrocyte-secreted basal lamina merge to form a common cerebrovascular basal lamina. This sets close contacts between the ECs, pericytes, and astrocytes. Mature astrocytes vary in density by brain region and display regional heterogeneity in morphology [52, 8]. Interconnected via gap junctions, they form a topologically distinct network that ensheathes through astrocytic perivascular endfeet processes, 99.7% of the capillary network and, concurrently, through its peri-synaptic processes, enwraps pre- and post-synaptic terminals of neurons, forming *tripartite synapses* [21, 101, 170, 117]. These provide efficient connections between the neuronal, astrocytic, and vascular networks and drive neurovascular coupling within the NGVU [119, 77, 142]. Astrocytes, ECs, and pericytes sense signaling within NGVUs and adjust CBF according to metabolic demands. The release of glutamate (Glu) and adenosine triphosphate (ATP) at the tripartite synapse triggers an influx of extracellular  $\text{Ca}^{2+}$  to astrocytes. The increase in cytosolic  $\text{Ca}^{2+}$  activates the release of gliatransmitters. Their biological effects depend on the site of action, the types of activated receptors, and the ligand concentration. Thus, nitric oxide (NO) and epoxyeicosatrienoic acid have been shown to produce strong capillary vasodilation. 20-hydroxyeicosatetraenoic acid, prostaglandin E2, and  $\text{Ca}^{2+}$  ions have potent vasoconstrictive [15, 112, 165], while astrocyte-derived ATP and its metabolite adenosine exhibit bidirectional effects on the capillary wall [182, 58, 110]. Intriguingly, astrocytes can also perceive changes in capillary blood pressure and, in turn, amend neuronal firing activity [97, 98]. This vasculo-neuronal hypothesis may present a mechanism through which body state can dictate, or at least modulate, brain function [121, 59, 142]. ECs react to changes in intracapillary pressure/flow and wall shear stress by releasing NO, endothelial factor-1, prostacyclin, and proteases. These cause pericyte relaxation, break up the extracellular matrix, induce vascular remodeling, and neovascularization that alter CBF to meet urgent requirements.

The study of nonlinearity, sensitivity to initial and state variables, stochasticity, and chaotic behavior of the NGVU is central to understanding and identifying the key determinants of the (patho)physiology of the brain. Mathematical modelling of NGVUs has witnessed impressive advances within the last decade due to an explosion in the amount and quality of experimentally available data. Two broad classes of models have emerged, i.e., i) neuron abstract, and ii) neuron morphologically and physiologically extended network models. While the first class captures essential architectural and electrical neuronal features, the second class accentuates the internal physiological signal processing underlying the repertoire of electrical activity observed *in vivo*. The number of publications on the subject is continuously increasing and it is beyond our scope to cite and evaluate critically each model and their produced results. We rather consider it the reader's responsibility to stay updated on progress in the field while exercising thorough impartial scientific judgment regarding the veracity, biological plausibility, and significance of the models. From our literature review, we conclude that at the time of writing there are no models of the NGVU that capture its role as a fundamental morpho-functional unit of the human brain. Current models, without exception, are based on fragmentary analyses

of constitutive components, and not a holistic representation of the unit with its complex biology. Consequently, these models do not support investigations or provide answers to questions about the brain’s perception and cognition in health and disease [47, 28]. To address this gap, we introduce a 3D-1D-0D multiscale computational tool designed to simulate the dynamics of the NGVU in a more integrated manner. Our model is built upon established biological principles and existing research, with validation currently focused on qualitative alignment with these foundations. However, due to the complexity of the system and the limitations of available experimental data, full quantitative validation remains a future direction to enhance the model’s predictive accuracy.

Within this study, we direct our attention to the dorsal vagal complex (DVC), a key brainstem structure located in the medulla oblongata. The DVC plays a pivotal role in autonomic control by integrating visceral sensory and motor signals that regulate parasympathetic outflow to the cardiovascular, respiratory, and gastrointestinal systems [113]. It works closely with neighboring nuclei, including the nucleus tractus solitarius (NTS), to coordinate reflexes such as baroreception (blood pressure regulation) and gut motility. Because the DVC must respond rapidly to changing homeostatic demands, studying its local neuro-glia-vascular interactions is especially relevant [41]. Fluctuations in autonomic activity require fine-tuned mechanisms to ensure adequate blood flow and metabolic support, making the DVC an ideal site for investigating the core principles of multicellular coordination in the brainstem [34, 29]. To facilitate a clearer understanding of our multi-scale modeling framework, Figure 1 provides a schematic illustration that depicts the stepwise construction of the model—from the macrovascular network (including the carotid, vertebral arteries and the circle of Willis), through the mesoscale arterial tree, to the microvascular unit representing a capillary vessel in the DVC, and finally the integration of the quadripartite synapse model with dynamic vessel radius regulation. By focusing on this region, we also hope to shed light on how disruptions in these processes could contribute to disorders affecting autonomic functions.

The aim of this paper is to provide a modular framework for constructing a comprehensive *in silico* model of the NGVU, which represents the first integrated model of its kind for the DVC. We begin with a gliovascular module in which astrocytic glia supports the function of associated cerebrovascular segments. A brief background of the major biological components that justify the working assumptions underlying our mathematical modelling of the essential physiological processes is presented in Section 2. This is followed by a description of a spatiotemporal computational model of the NGVU in Section 3, which includes discussions of the blood flow model, the quadripartite synapse model, the components of the neurovascular coupling model, and their integration. Numerical simulation results are presented in Section 4. Section 5 discusses the findings and Section 6 summarizes the contributions and suggests directions for future research. For a concise visual summary of our approach and its novelty, see the Graphical Abstract in Figure 2.

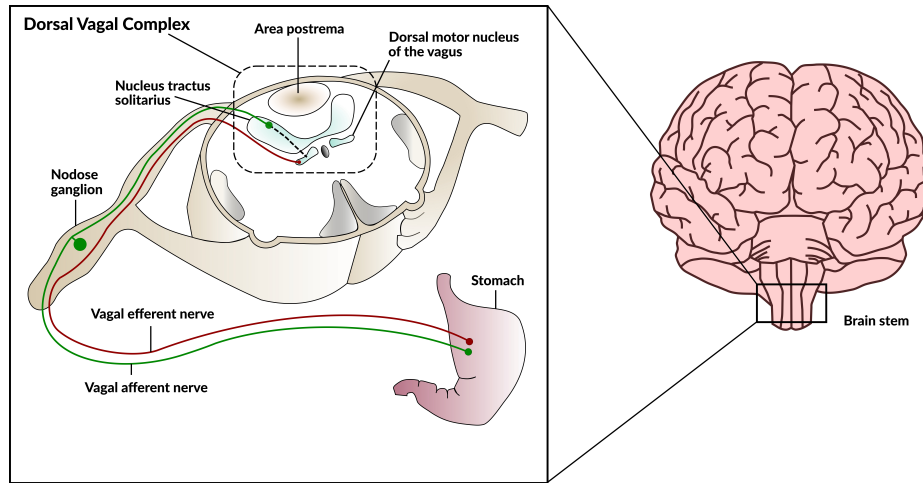


Fig. 1: Schematic representation of the dorsal vagal complex. A detailed view of the dorsal vagal complex is depicted, including the stomach, vagal afferent and efferent nerves, nodose ganglion, nucleus tractus solitarius, area postrema, and the dorsal motor nucleus of the vagus (adapted from [173]).

## 2 Biological Foundations of Neuro-Glial-Vascular Interactions

### 2.1 Anatomical and Morphological Components of the NGVU

The NGVU consists of structurally and functionally interconnected components essential for modeling brain physiology. Key elements include neurons, glial cells (especially astrocytes), SMCs, ECs, and blood vessels. These components work in concert to regulate cerebral blood flow, vascular tone, and neural activity, making their anatomical, morphological, and physiological characteristics vital for constructing a biologically accurate mathematical model.

Neurons, the fundamental morphological and functional units of the brain, number approximately  $10^{11}$  in the adult human brain. Structurally, they comprise the soma, axon(s), dendrites, nerve terminals, and spine buds [78]. The soma, measuring  $3\ \mu\text{m}$  to  $18\ \mu\text{m}$  in diameter [30], contains essential organelles such as the nucleus, endoplasmic reticulum (ER), mitochondria, and ribosomes, which sustain neuronal functionality [183, 4]. Axons, cylindrical extensions of the soma, have diameters ranging from  $0,1\ \mu\text{m}$  to over  $10\ \mu\text{m}$  and lengths of  $20\ \mu\text{m}$  to  $200\ \mu\text{m}$ , with collateral branches exceeding  $10\ \mu\text{m}$  [106, 148]. They end in nerve terminals or terminal boutons, about  $1\text{--}2\ \mu\text{m}$  in diameter [183]. Axons can be myelinated or unmyelinated, depending on the presence of a myelin sheath [183, 148]. Dendrites (from Greek *δένδρον*, meaning *tree*) are shorter, thinner processes branching from the soma, characterized by spine buds ( $0.5\text{--}2\ \mu\text{m}$  in diameter) connected by a spine neck ( $0.04\text{--}1\ \mu\text{m}$  long) [75]. Unlike axons, dendrites have a poorly developed cytoskeleton and fewer neurofilaments but are rich in microtubules and microfilaments. The nerve terminals and spine buds are key sites for synaptic connections (from Greek *σύναψις*, meaning *conjunction*) [144], consisting of a presynaptic

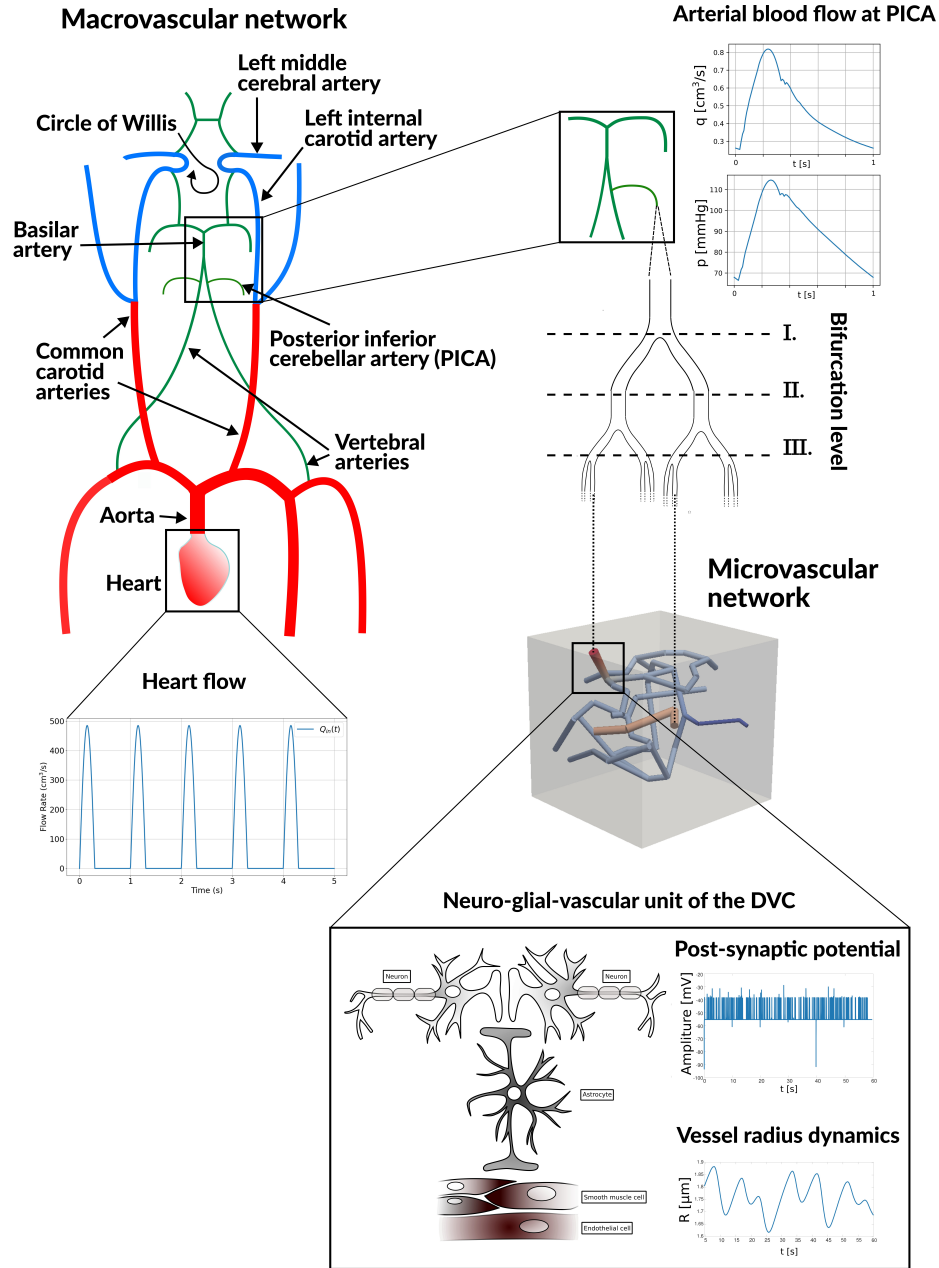


Fig. 2: Graphical Abstract. Schematic overview of our novel multiscale modeling framework for the NGVU in the DVC. The top panel shows the heart generating a pulsatile blood flow at one beat per second that is transmitted through major arteries including the common carotid, vertebral, and internal carotid arteries and collected in the circle of Willis. The arterial blood then enters the posterior inferior cerebellar artery (PICA) to supply the DVC via a series of symmetric bifurcations in the mesoscale arterial tree. The bottom panel shows a detailed view of the local neuro-glial-vascular unit where the quadripartite synapse model captures interactions among excitatory and inhibitory neurons, astrocytes, and vascular smooth muscle cells. This integration dynamically regulates vessel radius and optimizes oxygen delivery to surrounding tissue through a one-dimensional to three-dimensional coupling approach.

terminal, a synaptic cleft (20–30 nm), and a postsynaptic terminal. These connections form between neurons, astrocytes, or combinations thereof via dendritic, axonal, axo-dendritic, and axo- or dendro-somatic synapses [183].

Astrocytes, oligodendrocytes, microglia, and radial cells belong to the class of glial cells [78, 183]. Astrocytes are star-shaped cells with a relatively small soma measuring 10–20  $\mu\text{m}$  [183]. Six or more major branches extend from the soma, further dividing into branchlets and leaflets, with cross-sectional diameters ranging from 10 to 100 nm [24, 5]. Morphologically, astrocytes are categorized into two types: fibrous, found in white matter, and protoplasmic, located in gray matter. Both types feature fewer organelles and unbranched processes up to 300  $\mu\text{m}$  in length [4, 70]. The process endings, known as endfeet, form astro-dendritic, astro-axonal, and neuron-smooth muscle synapses within the NGVU [92, 66, 158]. Astrocytes possess a well-developed ER, which serves as the primary intracellular  $\text{Ca}^{2+}$  store, along with numerous mitochondria and an extensive microfilament network [156, 155].

Smooth muscle cells form the walls of cerebral blood vessels [183]. These fusiform-shaped cells measure approximately 20  $\mu\text{m}$  in length and 6  $\mu\text{m}$  in width, playing a crucial role in regulating vascular tone and providing mechanical elasticity to the vascular wall [80, 177]. SMCs form a syncytium through multiple gap junctions and basal laminae invaginations [183]. Their contractile apparatus comprises contractile proteins, regulatory proteins, and a cytoskeleton. The primary contractile proteins are actin and myosin, organized into thin and thick filaments (myofilaments). Thin filaments, approximately 7 nm in diameter, consist mainly of actin, while thick filaments, measuring 12–15 nm in diameter, are predominantly composed of myosin. Regulatory proteins such as myosin light-chain kinase (MLCK), myosin light-chain phosphatase (MLCP), calmodulin (CaM), and caldesmon, along with the intracellular arrangement of myofilaments, constitute the functional contractile apparatus [183, 26].

The luminal surface of blood vessels is lined with a monolayer of ECs, forming a selective semi-permeable membrane that regulates the movement of small molecules ( $\text{O}_2$ ,  $\text{CO}_2$ ,  $\text{H}_2\text{O}$ ) and ions ( $\text{Ca}^{2+}$ ,  $\text{K}^+$ ) between the blood and brain parenchyma. These cells also modulate cerebral blood flow, vascular tone, inflammation, thrombosis, and adhesion. Endothelial dysfunction is a key factor in the pathogenesis of cerebral small vessel disease [183, 163]. ECs synthesize and release vasoactive mediators, including NO, endothelium-derived hyperpolarizing factor (EDHF), eicosanoids, and endothelin-1 (ET-1), to regulate vascular tone. NO and EDHF act as potent vasodilators by influencing the contractile apparatus and membrane hyperpolarization of SMCs, while eicosanoids and ET-1 function as vasoconstrictors, inducing intense smooth muscle contractions [65, 109].

Calcium ions act as crucial secondary messengers in regulating endothelial cell processes. Under physiological conditions, ECs maintain a low cytosolic  $\text{Ca}^{2+}$  concentration (100  $\text{nmol L}^{-1}$ ) compared to the extracellular concentration of 1.5–2  $\text{mmol L}^{-1}$  in the brain. Cytosolic  $\text{Ca}^{2+}$  is essential for the synthesis and release of endothelium-derived factors, including NO. Agonist-driven NO release, such as by acetylcholine, is mediated by intracellular  $\text{Ca}^{2+}$  oscillations. Mechanical stimuli sensed by mechanosensitive ion channels elevate intracellular  $\text{Ca}^{2+}$  levels, leading to endothelium-dependent smooth muscle hyperpolarization and relaxation. Additionally, reactive oxygen species

produced by ECs can activate transient receptor potential (TRP) channels, triggering  $\text{Ca}^{2+}$  influx and dilating cerebral arteries [168, 3].

## 2.2 Transmitter, Ion Channels and Electrical Signal Transduction

The NGVU relies on various electrochemical processes to facilitate neural communication and vascular regulation. These processes are driven by the coordinated action of neurotransmitters, ion channels, and second messengers, which underlie the generation and propagation of signals across neurons, astrocytes, and vascular components. Understanding the dynamics of these signaling mechanisms is essential for modeling the complex interactions within the NGVU, as they regulate neural activity, synaptic transmission, and vascular tone in both physiological and pathological conditions.

Transmitters are essential for the electrochemical processing of information at chemical synapses in the NGVU. Glu, the primary excitatory neurotransmitter, is used by nearly 90% of neurons and accounts for 80–90% of brain synapses. Synthesized *de novo* from glucose or via glutamine recycling, Glu is stored in vesicles and released by exocytosis [78]. In the synaptic cleft, Glu binds to ionotropic receptors (N-methyl-D-aspartate (NMDA),  $\alpha$ -amino-3-hydroxy-5-methyl-4-isoxazolepropionic acid (AMPA), and kainate) to alter ion channel permeability or to metabotropic receptors, which regulate intracellular signaling via G-proteins [147, 120].  $\gamma$ -aminobutyric acid (GABA), the primary inhibitory neurotransmitter, is synthesized via the GABA-shunt and operates through ionotropic GABA<sub>A</sub> and metabotropic GABA<sub>B</sub> receptors. GABA<sub>A</sub> activation causes  $\text{Cl}^-$  influx and hyperpolarization, while GABA<sub>B</sub> reduces  $\text{Ca}^{2+}$  influx and increases  $\text{K}^+$  efflux, inhibiting cell excitability [78, 104]. NO, a gaseous transmitter synthesized on demand by NO synthases, diffuses freely due to its solubility in fat and water [2, 61]. Despite its short half-life (2 ms intravascularly and up to 2 s extravascularly), NO mediates significant physiological effects, including smooth muscle relaxation and vasodilation [44, 67]. Endothelial cell-derived NO primarily drives vasorelaxation during rest, while neuronal NO dominates during activation, influencing arteriolar diameter by diffusing into SMCs [44]. NO release, triggered by wall shear stress, delays the return of arteriolar radius to baseline [166]. Together, Glu and NO mediate excitatory synaptic signaling and vascular regulation, while the interplay with inhibitory GABA ensures neural and vascular homeostasis in the NGVU [14, 78, 44].

In addition to signaling molecules, second messengers play a crucial role in intracellular signal transmission by forming after the binding of signaling molecules to membrane-bound or cytosolic receptors [78]. Inositol trisphosphate ( $\text{IP}_3$ ), a cyclic compound derived from membrane phospholipids during the  $\text{IP}_3$  pathway, triggers  $\text{Ca}^{2+}$  release from the ER [78]. ATP, apart from serving as an energy source, acts as a second messenger by binding to purinergic receptors and is co-localized with other neurotransmitters [78]. In astrocytes, ATP facilitates  $\text{Ca}^{2+}$  wave propagation and is released in a  $\text{Ca}^{2+}$ -dependent manner or through lysosome exocytosis, hemichannels, and anion channels [179, 107, 94]. Cellular membranes, composed of amphiphilic lipid bilayers with hydrophilic head groups facing outward and hydrophobic tails inward, serve as structural barriers enabling the exchange of substances between cells and their environment [78, 19]. Ion channels, integral membrane proteins, facilitate the passage of ions

like  $\text{Na}^+$ ,  $\text{K}^+$ ,  $\text{Ca}^{2+}$ , and  $\text{Cl}^-$  across the lipid bilayer through selective water-filled pathways, achieving transport rates of  $10^7$ – $10^8$  ions per second and forming the basis of cellular excitation [19].

The movement of ions is driven by two primary forces: the concentration gradient and the potential difference. Passive transport occurs along an electrochemical gradient, with the ion current determined by the channel's conductivity and open probability. Greater membrane potential amplitude increases the driving force and current amplitude. Depending on channel type, ion concentration, and temperature, ion channel conductivities range from 1 to  $10^{-10}$  S, while specific membrane resistances vary from  $10^{12}$  to  $10^9 \Omega$  [19]. Neurons of the NGVU model express voltage-dependent  $\text{Na}^+$  channels, L-type and N-type  $\text{Ca}^{2+}$  channels,  $\text{Cl}^-$  channels, and large conductance  $\text{Ca}^{2+}$ -dependent  $\text{K}^+$  channels (BK) [68]. Calcium-induced calcium release (CICR) facilitates  $\text{Ca}^{2+}$  release from intracellular stores [18], while voltage-operated calcium channels (VOCC) mediate calcium entry during depolarization, crucial for neurotransmitter release and muscle contraction [154]. Other critical ion transporters include inward-rectifying potassium channels (KIR), which regulate the resting membrane potential [79], the sodium bicarbonate pump (NBC) for pH and ion homeostasis [11], and the potassium chloride co-transporter pump (KCC1) for cell volume regulation [146]. Neuronal communication relies on electrical potentials, with dendrites transmitting signals to the soma, where action potentials are generated [78, 19]. Action potentials involve sequential phases: overcoming the threshold potential, rapid depolarization (upstroke and overshoot), repolarization, and post-hyperpolarization, mediated by  $\text{Na}_v$ -channels for depolarization and  $\text{K}_v$ -channels for repolarization [19].

Axons and dendrites function as biological cables composed of capacitor-resistor elements, with distinct roles in neural signal processing. In dendrites, the membrane time constant and length constant govern the integration and conduction of synaptic potentials to the soma, while axons employ active mechanisms to propagate action potentials [19]. Unmyelinated axons typically conduct action potentials at approximately 1 m/s, with conduction speed increasing as axonal diameter grows, reducing internal resistance. Human unmyelinated nerve fibers generally have a diameter of around  $1 \mu\text{m}$ , allowing continuous excitation propagation along the axon to the synapse [19]. At chemical synapses, electrical signals are converted into chemical reactions mediated by neuro- and gliotransmitters [78]. Synaptic transmission involves a sequence of events: nerve terminal depolarization,  $\text{Ca}^{2+}$  influx via VOCC, diffusion of  $\text{Ca}^{2+}$  to vesicular active sites, neurotransmitter release into the synaptic cleft, receptor binding on the postsynaptic membrane, activation of ion channels or second messenger systems, and either depolarization or hyperpolarization of the postsynaptic membrane [19].

### 2.3 Physiology of Vasoconstriction, Autoregulation and Bioenergetics

Understanding the physiology of vasoconstriction, autoregulation, and bioenergetics is essential for accurately modeling the dynamic interactions within the NGVU. These processes govern the regulation of cerebral blood flow, vascular tone, and intracellular energy metabolism, forming the basis for predictive models of brain function. By incorporating these mechanisms, models can capture the physiological responses to neural

activity, systemic changes, and metabolic demands, enabling deeper insights into neurovascular coupling and brain homeostasis.

SMCs in the blood vessel wall form a syncytium and rely on post-translational modifications for contraction due to the absence of intrinsic myosin ATPase activity. Contraction is regulated by MLCK, a  $\text{Ca}^{2+}$ /CaM-dependent kinase activated by free  $\text{Ca}^{2+}$ , which phosphorylates myosin, enabling actin-myosin interaction and force generation [88, 45, 183]. Caldesmon, bound to actin-tropomyosin, is displaced upon  $\text{Ca}^{2+}$ -CaM binding, facilitating this interaction. MLCP counteracts MLCK activity, its regulation mediated by Rho-kinase inhibition or stimulation via NO through cyclic guanosine monophosphate (cGMP) and cyclic adenosine monophosphate (cAMP) production [133]. SMCs integrate inputs from neurons, astrocytes, and ECs, primarily via  $\text{Ca}^{2+}$  transport and voltage coupling. Their contraction or relaxation modulates vessel radius, driving vasoconstriction or dilation and playing a critical role in neurovascular regulation within the NGVU [45, 133].

The cardiovascular system, consisting of the heart and blood vessels, facilitates the transport and exchange of oxygen ( $\text{O}_2$ ), carbon dioxide ( $\text{CO}_2$ ), nutrients, electrolytes, and hormones [183]. Arteries carry blood away from the heart, while veins return it, with arterioles, capillaries, and venules connecting these pathways. The aorta branches into progressively smaller arteries, forming a vascular tree where vessel diameters decrease while cross-sectional area increases. Vessel walls have three layers: the tunica intima, lined with ECs for adhesion and coagulation; the tunica media, containing SMCs and elastic fibers to regulate diameter; and the tunica externa, made of connective tissue [183]. Arteries can measure up to 3 cm, arterioles are under 30  $\mu\text{m}$ , and capillaries are 5–8  $\mu\text{m}$  wide, optimizing exchange due to their large cross-sectional area and a flow rate of 0,5  $\text{mm s}^{-1}$  [183, 180]. Four major arteries, including the internal carotid and vertebral arteries, supply the brain. Capillaries, spanning 644 km with a surface area of 20  $\text{m}^2$ , consist of ECs, a basal lamina, and pericytes. Smooth muscle layers in larger arteries reduce to a single layer in capillaries, where pericytes replace SMCs, separated from astrocytes by the perivascular space [150, 9, 184].

Autoregulation maintains nearly constant CBF within a range of 50 mmHg to 160 mmHg by adjusting vascular tone to ensure oxygen and nutrient delivery [48, 46, 84]. CBF is driven by cerebral perfusion pressure (CPP), defined as the difference between mean arterial pressure (MAP) and intracranial pressure (ICP), and cerebral vascular resistance (CVR) [142]. CPP typically ranges from 60 mmHg to 80 mmHg, while normal ICP is 5 mmHg to 10 mmHg and has less impact on CPP than MAP [142]. MAP, averaging blood pressure over one cardiac cycle, normally ranges from 70 mmHg to 100 mmHg but fluctuates with activity, stress, or other systemic factors [123]. Autoregulation alters vessel diameter through vasodilation (increased diameter) or vasoconstriction (decreased diameter) [137, 140]. However, its range is limited to  $\pm 20$  mmHg from baseline with a latency of 60 s [31]. Sudden or extreme arterial pressure (AP) changes induce passive CBF variations. Elevated AP increases intracellular  $\text{Ca}^{2+}$  in SMCs, activating MLCK and triggering actin-myosin crosslinking, resulting in smooth muscle contraction and vasoconstriction [150, 140]. Systemic factors such as posture, glucose levels, hormones, hematocrit, blood viscosity, and cold stress also influence CBF, engaging the cerebrovascular tree with segmental specificity [31, 6].

Intracellular nutrient metabolism is fundamental for brain function, driven by biochemical pathways that depend on the delivery of glucose and oxygen, regulated by neuro-glial activity. Within cells, mitochondria play a central role in energy production through enzymatic reactions, essential for eukaryotic cells such as neurons, astrocytes, ECs, and SMCs [36]. Metabolic pathways include glycolysis, glycogenolysis, the pentose phosphate and polyol pathways,  $\beta$ -oxidation, the tricarboxylic acid (TCA) cycle, ATP synthesis, ionic and redox-energy transducing processes, and reactive oxygen species (ROS) generation and scavenging [36]. ATP is synthesized via glucose catabolism through glycolysis, the TCA cycle, and oxidative phosphorylation, where nicotinamide adenine dinucleotide (hydrogen) (NADH)-driven proton gradients power ATP generation [152]. Glycolysis produces ATP both anaerobically and aerobically, generating pyruvate for the TCA cycle and intermediates for anabolic pathways [25]. Glycogenolysis breaks glycogen into glucose-1-phosphate and glucose, providing a key glycogen utilization pathway [132]. The pentose phosphate and polyol pathways support biosynthetic metabolism and redox homeostasis [161]. The ATP cycle, involving eight enzymes, links pyruvate and malate oxidation to  $\text{CO}_2$  production and NADH generation, sustaining mitochondrial respiration and metabolic functions [56, 57].  $\beta$ -oxidation of polyunsaturated fatty acids (PUFAs) balances energy demand, competing with glucose as a primary oxidative substrate [69]. Ionic and redox-energy transducing processes couple biochemical systems through electronic energy transitions [111]. ROS generation and scavenging involve oxygen radicals and oxidizing agents, influencing metabolism, mitochondrial electron transport, signal transduction, and gene expression [7].

### 3 Neuro-Glial-Vascular Unit Model

#### 3.1 Blood flow model

In order to determine the blood supply of a NGVU, we consider a capillary network contained in a block measuring  $150 \times 160 \times 140 \mu\text{m}$ . It is based on a three-dimensional vascular network reconstructed from scanning electron microscopy (SEM) data of the rat brain. The vascular structure, originally presented by [122], highlights the terminal vascular bed in the superficial cortex. The reconstruction and its application to oxygen transport simulations were detailed by [151]. This dataset, denoted by *brain99*, provides geometric and flow data for a vascular block  $\Omega \subset \mathbb{R}^3$  measuring  $150 \times 160 \times 140 \mu\text{m}$ , including information on vessel radii, lengths, and Cartesian coordinates.

The data set *brain99* is utilized as a representative microcirculation block for the DVC. At the inlets of the capillary vessels with the two largest inlets, coupling between macro- and microcirculation is applied, ensuring a physiologically consistent transition of flow and pressure between arterial and capillary blood vessel networks. For this purpose, we prescribe at the respective inlets flow rates derived from a model for blood flow in a network composed of larger arteries. The network, which is considered in this work can be seen in Figure 3. It consists of the largest arteries attached to the heart, as well as the brachial and carotid arteries, and the circle of Willis. This network is enhanced by two arteries that branch out from the vertebral arteries (Vessel 35 and 37 in Figure 3). Moreover, the vertebral arteries are split into two parts, where the distal parts are considered as new vessels. The four additional vessels are labeled with the indices 34, 35,

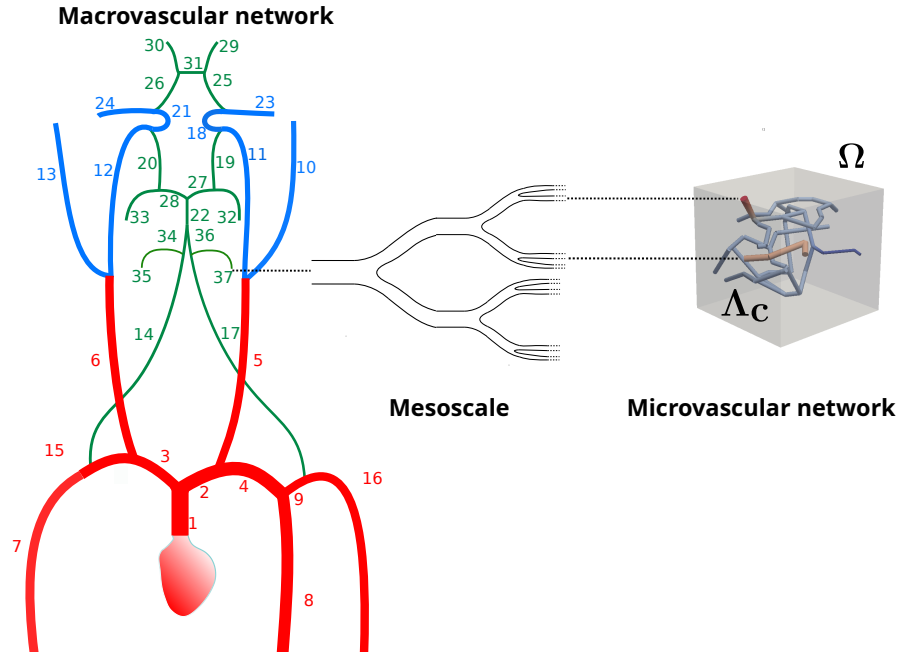


Fig. 3: This figure gives an overview on the vascular systems that are considered for simulating blood flow from the heart to the neuro-glial-vascular unit. The macrovascular network and mesoscaled network are part of the arterial tree, while the microvascular network has to be assigned to the capillaries. By means of the macrovascular network, we determine the amount of blood volume transported towards the head in particular through the vertebral arteries. The mesoscaled network connects one of the vertebral arteries with the capillary network  $\Lambda_c$  supplying our neuro-glial unit contained in  $\Omega$ .

36 and 37. In the remainder of this work, this network is referred to as a macrovascular network. We assume that  $\Omega$  is supplied by Vessel 37. In order to connect  $\Omega$ , we use an averaged flow rate at the outlet of Vessel 37 as input for a simple model representing the vessel tree linking Vessel 37 and the capillary network  $\Lambda_c$  contained in  $\Omega$ . This vessel tree comprises a part of the mesoscale within the vascular tree. An output of the mesoscale model, we obtain two flow rates that are prescribed at the inlets of the vessels with the two largest radii (see Figure 3). All in all we obtain a multi-scale model for a flow path starting at the inlet of the aorta and ending in the NGVU contained in  $\Omega$ .

In the following, we describe the different components of our model: In a first subsection, a dimension-reduced model for flow in the macrovascular network is presented. Next, a flow model within the microvascular network is described. Finally, a strategy for coupling both models via a model for the mesoscale is discussed.

### 3.1.1 Blood flow model for the macrovascular network

For the macrovascular network we use the one-dimensional model (1D) described in [23,

83] and [38, Chapter 2] on each vessel. Hence, we determine the vessel area  $A$  [cm<sup>2</sup>], and flow rate  $Q$  [cm<sup>3</sup>s<sup>-1</sup>] on the center line  $\Lambda$  of a blood vessel with length  $L$  [cm].  $\Lambda$  is parameterized by a variable  $z \in [0, L]$ .  $A$  and  $Q$  are solutions of a non-linear hyperbolic system of equations given by [102, Section 3.2]:

$$\partial_t A + \partial_z Q = 0, \quad z \in (0, L), \quad t > 0, \quad (1)$$

$$\partial_t Q + \partial_z \left( \frac{Q^2}{A} \right) + \rho^{-1} A \partial_z P = -2 \cdot (\bar{\gamma} + 2) \cdot \frac{\mu(2 \cdot R)}{\rho} \cdot \frac{Q}{A}, \quad z \in (0, L), \quad t > 0, \quad (2)$$

where  $t$  [s] is the time variable and  $\rho = 1.028 \cdot 10^{-3}$  g cm<sup>-3</sup> represents the fluid density.  $\mu$  [Pa s] is a function describing the viscosity depending on the vessel radius  $R$  [cm]. The formula for this function can be found in [143].  $\bar{\gamma} = 9$  is a shape parameter for the flow profile ([38, Cp. 2 & Sec. 6.1]). The pressure is related to the vessels by a fluid-structure interaction model, which is known as the Young-Laplace equation [130, 167]:

$$P = G_0 \left( \sqrt{\frac{A}{A_0}} - 1 \right).$$

The parameter  $G_0$  is given by:

$$G_0 = \frac{\sqrt{\pi} \cdot h_0 \cdot E}{(1 - \nu^2) \cdot \sqrt{A_0}}.$$

$h_0$  [cm] is the wall thickness,  $E$  [Pa] the elastic modulus,  $\nu = \frac{1}{2}$  is the Poisson ratio and the vessel area for  $P = 0$  is denoted by  $A_0$  [cm<sup>2</sup>]. The radius of  $A_0$  is given by  $R_0$  [cm].

A table containing the values for  $L$ ,  $h_0$ ,  $E$  and  $R_0$  can be found in [1, Table 1]. In this table one can find the data for Vessel 1-33 apart from the lengths of Vessel 14 and 17. The missing data for Vessel 34 to 37 as well as Vessel 14 and 17 can be listed in Table 1.

Vessel	$L$ [cm]	$R$ [cm]	$h_0$ [cm]	$E$ [10 <sup>6</sup> · Pa]
14	9.866	0.136	0.034	0.8
17	9.866	0.136	0.034	0.8
34	4.930	0.136	0.034	0.8
35	6.000	0.080	0.034	0.8
36	4.930	0.136	0.034	0.8
37	6.000	0.080	0.034	0.8

Table 1: Parameters for Vessel 14 and 17 as well as Vessel 34 to 37.

At the bifurcations of the network, we enforce continuity of the total pressure and flow conservation. The heart beats are emulated by describing the flow rate at the inlet of the

aorta (Vessel 1) by a half-sine wave. We denote this flow rate by  $Q_{in}$  [ $\text{cm}^3\text{s}^{-1}$ ]. It is given by the  $T$ -periodic extension of

$$Q_{in}(t) = \begin{cases} Q_{\max} \sin\left(\frac{\pi t}{0.3 \cdot T}\right), & \text{for } 0 \leq t \leq 0.3 \cdot T \\ 0, & \text{for } 0.3 \cdot T < t \leq T. \end{cases}$$

In case of our simulations, we set  $T = 1.0$  s and  $Q_{\max} = 485.0$   $\text{cm}^3\text{s}^{-1}$ . The influence of the omitted vasculature beyond the outlets is accounted for by a zero-dimensional (0D) Windkessel model [64]. To calibrate the Windkessel parameters, a method described in [102, Section 3.6.2] is used. All in all, this results in a 1D-0D coupled model.

### 3.1.2 Blood flow model for the microvascular network

Modeling blood flow in a capillary network, we use a stationary description relating the 1D pressures  $p_1$  on the capillary centerlines  $\Lambda_c$  with the 3D pressures  $p_3$  in the surrounding space  $\Omega$ :

$$-R^2 \pi \partial_s (K_1 \partial_s p_1) + 2\pi R L_p (p_1 - \Pi_\Omega p_3) = 0 \quad \text{on } \Lambda_c, \quad (3)$$

$$-\nabla \cdot (K_3 \nabla p_3) + L_p (p_3 - \Pi_\Lambda p_1) \delta_\Gamma = 0 \quad \text{on } \Omega, \quad (4)$$

where  $\Pi_\Lambda : \Lambda_c \rightarrow \Gamma$  extends functions on the center line to functions on the cylinder boundary,  $\Pi_\Omega : \Omega \rightarrow \Lambda$  averages functions on cylinder cross sections, and  $\delta_\Gamma$  the Dirac distribution on the cylindrical vessel walls. By this, we obtain a 3D-1D coupled model.  $R$  describes the radius of the vessels and  $L_p$  is the permeability of the vessel walls. Moreover  $K_1 = R^2/8\mu(2-R)$  and  $K_3$  are the permeabilities of the vessel and the medium contained in  $\Omega$  (see [103] for details). As in Section 3.1.1, the viscosity function  $\mu$  is taken from [143]. This flow model yields flow velocities in the capillary network  $\Lambda_c$  and  $\Omega$ , which are denoted by  $v_c$  and  $v_\Omega$ . The velocities are computed as follows:

$$v_c = -K_1 \partial_s p_1 \text{ and } v_\Omega = -K_3 \nabla p_3.$$

Using these velocities, convection diffusion equations are formulated to model the transport of oxygen, nutrients and other substances within  $\Lambda_c$  and  $\Omega$ . As in case of the flow model there is a 1D PDE for the transport in the capillary network and a 3D PDE for the corresponding processes in the surrounding medium. For further information, we refer to [103]. At the boundary of  $\Omega$  we set homogeneous Neumann boundary conditions. The boundary conditions for  $\Lambda_c$  are discussed in the next subsection.

### 3.1.3 Coupling of macro- and microcirculation

To couple the macrocirculation with the microcirculation, we assume that the inlets in our capillary bed are connected to the outlet of Vessel 37 by a surrogate model for the arterial tree between the capillary network and the outlet of Vessel 37 (see Figure 3). As in [64], it is assumed that these arterial trees are symmetric. This means that every vessel bifurcates into two child vessels following Murray's law [124, 125], and additionally, both child vessels have the same radii. Vessel radii between two arbitrary bifurcation levels  $l$  and  $l + 1$  are thus related by

$$r_l = 2^{1/\gamma} r_{l+1},$$

where  $\gamma \in [2, 3.5]$ . If  $n$  bifurcations are given, we  $r_0$  and the final radius  $r_n$  are related to each other as follows:

$$r_0 = 2^{n/\gamma} r_n.$$

The number of levels in our arterial tree is thus given by

$$n = \log_2(r_0/r_n)^\gamma.$$

Assuming that the flow  $Q_l$  at level  $l$  is evenly divided at each bifurcation yields the relationship  $Q_l = 2Q_{l+1}$ . This implies:

$$Q_0 = 2^n Q_n = \left(\frac{r_0}{r_n}\right)^\gamma Q_n.$$

Coupling the macro- and microcirculation, we replace  $r_0$  by the initial radius of Vessel 37:  $r_0 = R_{0,37}$ , while  $r_n$  is the radius of a capillary containing an inlet. In case of our capillary network  $\Lambda_c$ , we choose the vessels at the boundary with the two largest radii. The corresponding radii are denoted by  $r_{c,i}$ ,  $i \in \{1, 2\}$ . To compute  $Q_0$ , we simulate blood flow within the macrovascular network starting with  $A = A_0$  and  $Q = 0$  for each vessel. The simulation is stopped after the pressure and flow rate curves become periodic for each heart beat. If this is the case, we report the flow rate curve  $Q_{37}$  at the outlet of Vessel 37 for one heart beat i.e. for a time interval  $[t, t + T]$  and compute the average of  $Q_{37}$ . Finally, we equate  $Q_0$  and this average:

$$Q_0 = \frac{1}{T} \int_t^{t+T} Q(t) dt.$$

By this, the flow rates  $Q_{r_{c,i}}$  are given by:

$$Q_{r_{c,i}} = Q_0 \cdot \left(\frac{r_{c,i}}{R_{0,37}}\right)^\gamma$$

To ensure mass conservation, we distribute at the outlets of  $\Lambda_c$  the flow rate

$$Q_{in,c} = Q_{r_{c,1}} + Q_{r_{c,2}}$$

entering the network according to their section areas. Since we have on both inlets and outlets Neumann boundary conditions, we have to fix the pressure at some place of the network such that an average pressure of about 30 mmHg in  $\Lambda_c$  results. Otherwise the flow problem for  $\Lambda_c$  would be ill-posed.

### 3.2 Quadripartite Synapse Model

The quadripartite synapse model of the DVC incorporates the Glu-, GABA-, neurons and astrocytes. The neurotransmission involves Glu, GABA, AMPA, NMDA, GABA<sub>A</sub> and GABA<sub>B</sub> type receptors, as described in [20, 164]. The model encompasses a pre-synaptic bouton, a post-synaptic dendritic spine-head, SMCs, and a perisynaptic astrocytes that governs  $Ca^{2+}$  dynamics within the synaptic bouton. The calcium dynamics subsequently

influence Glu release in the SMCs. The model further accounts for Glu concentration within the SMCs, incorporating the process of Glu reuptake by astrocytes. We further incorporated GABA neurons which have similar dynamics to the Glu-neurons. In addition, NMDA, GABAa and GABAb receptors with similar dynamics as AMPA receptor are considered.

Neuronal activities have the ability to induce elevations in  $\text{Ca}^{2+}$  within astrocytes [55, 141], which in turn increases the concentration of  $\text{Ca}^{2+}$  in neighboring glial cells, including astrocytes, that express a wide range of receptors [129]. The activation of these receptors leads to an increase in astrocytic  $[\text{Ca}^{2+}]$  and the subsequent release of various transmitters such as Glu, GABA, d-serine, and ATP. The depletion of the releasable vesicle pool due to recent neurotransmitter release in response to pre-synaptic action potentials results in short-term synaptic depression [178, 20]. The proposed model is inspired by the experimental work conducted in [138], who utilized hippocampal slice preparations from immature Wistar rats. The computational framework presented here integrates various detailed biophysical models to emphasize distinct facets of neurons-astrocytes signaling.

### 3.2.1 Pre-synaptic Neuronal Action Potential and Bouton Calcium Dynamics

The generation of pre-synaptic action potential trains is achieved using the Hodgkin-Huxley formalism [81]. Elevation of  $\text{Ca}^{2+}$  concentration within the pre-synaptic bouton is modeled by incorporating both rapid influx, utilizing single protein properties [53], and slower dynamics through a modified Li-Rinzel model [108]. The initiation of the action potential occurs at the axon hillock of the pre-synaptic neurons. The generation of pre-synaptic action potentials in computational models has traditionally been accomplished using the Hodgkin-Huxley framework [126, 172]. Given that the details of pre-synaptic action potential generation are not the primary focus of the present study, we adopt the Hodgkin-Huxley model to simulate regular spiking and burst activity for simplicity, given by

$$\begin{aligned} C \frac{dV_{pre}}{dt} &= I_{app} - g_K n^4 (V_{pre} - V_K) - g_{Na} m^3 h (V_{pre} - V_{Na}) - g_L (V_{pre} - V_L), \\ \frac{dx}{dt} &= \alpha_x (1 - x) - \beta_x x, \quad x \in \{n, m, h\}, \end{aligned} \quad (5)$$

where  $V_{pre}$  denotes the pre-synaptic membrane potential, and  $I_{app}$  represents the applied current density. The conductances for potassium, sodium, and leak channels are given by  $g_K$ ,  $g_{Na}$ , and  $g_L$  respectively. Correspondingly,  $V_K$ ,  $V_{Na}$ , and  $V_L$  are the reversal potentials for potassium, sodium, and leak channels. The variables  $m$  denotes the sodium activation,  $h$  is the sodium inactivation, and  $n$  is defined as the potassium activation. The

expressions for  $\alpha_x$  and  $\beta_x$  for  $x = (m, h, n)$  are given by

$$\alpha_n = \frac{0.01(-V_{pre} - 60)}{\exp\left(\frac{-V_{pre}-60}{10}\right) - 1}, \quad \beta_n = 0.125 \exp\left(\frac{-V_{pre} - 70}{80}\right), \quad (6)$$

$$\alpha_m = \frac{0.1(-V_{pre} - 45)}{\exp\left(\frac{-V_{pre}-45}{10}\right) - 1}, \quad \beta_m = 4 \exp\left(\frac{-V_{pre} - 70}{18}\right), \quad (7)$$

$$\alpha_h = 0.07 \exp\left(\frac{-V_{pre} - 70}{20}\right), \quad \beta_h = \frac{1}{\exp\left(\frac{-V_{pre}-40}{10}\right) + 1}. \quad (8)$$

The action potential initiated at the axon hillock of the pre-synaptic neurons propagates along the axon to the terminal without degradation, causing an elevation in cytosolic  $[Ca^{2+}]$ . This increase in intracellular  $[Ca^{2+}]$  is composed of two parts:  $[Ca^{2+}]$  resulting from the action potential, denoted as  $c_{fast}$ , and  $[Ca^{2+}]$  originating from intracellular stores, denoted as  $c_{slow}$ , based on the kinetics speed. Thus, the total intracellular  $[Ca^{2+}]$ , represented as  $c_i$ , is defined as

$$c_i = c_{fast} + c_{slow} \rightarrow \frac{dc_i}{dt} = \frac{dc_{fast}}{dt} + \frac{dc_{slow}}{dt}. \quad (9)$$

The significant impact of rapid  $Ca^{2+}$  kinetics on neurotransmitter release is well documented [17]. For simplicity, the  $Ca^{2+}$  influx through the plasma membrane is modeled via N-type channels [175]. Immature cells, as described in [138], are assumed in this study. The equation governing  $[Ca^{2+}]$  resulting from the action potential follows a straightforward construction and degradation framework [96], which can be expressed as

$$\frac{dc_{fast}}{dt} = \underbrace{-\frac{I_{Ca}A_{btn}}{z_{Ca}FV_{btn}} + J_{PM,leak}}_{construction} - \underbrace{\frac{I_{PM,Ca}A_{btn}}{z_{Ca}FV_{btn}}}_{destruction}, \quad (10)$$

where  $I_{Ca}$  represents the  $Ca^{2+}$  current through an N-type channel,  $A_{btn}$  is the bouton's surface area,  $z_{Ca}$  is the valence of the  $Ca^{2+}$  ion,  $F$  is Faraday's constant, and  $V_{btn}$  is the bouton's volume. Additionally,  $I_{PM,Ca}$  denotes the current attributed to the electrogenic plasma membrane  $Ca^{2+}$  ATPase, which expels excess  $Ca^{2+}$  from the cell [90]. The function of this pump is described using a standard Michaelis-Menten type formalism [53]. Furthermore,  $J_{PM,leak}$  accounts for the positive leak of  $Ca^{2+}$  from the extracellular space into the bouton, ensuring that the Michaelis-Menten pump does not reduce cytosolic  $Ca^{2+}$  to zero [16]. The  $Ca^{2+}$  current through the N-type channel is modeled at the single protein level [53] as

$$I_{Ca} = \rho_{Ca} m_{Ca}^2 \underbrace{g_{Ca}(V_{pre}(t) - V_{Ca})}_{single\ open\ channel}, \quad (11)$$

where  $\rho_{Ca}$  represents the density of N-type channel proteins, determining the number of  $Ca^{2+}$  channels present on the bouton membrane. The parameter  $g_{Ca}$  denotes the conductance of a single N-type channel, while  $V_{Ca}$  is the reversal potential for the  $Ca^{2+}$  ion,

given by the Nernst equation [96] as

$$V_{Ca} = \frac{RT}{z_{Ca}F} \ln \left( \frac{c_{ext}}{c_i^{rest}} \right), \quad (12)$$

where  $R$  denotes the universal gas constant,  $T$  is the absolute temperature,  $c_{ext}$  represents the extracellular  $Ca^{2+}$  concentration, and  $c_i^{rest}$  signifies the resting total intracellular  $[Ca^{2+}]$ . It is assumed that each N-type channel is composed of two gates, with  $m_{Ca}$  indicating the probability of a single gate being open. Therefore, the probability of a single N-type channel being open, which requires both gates to be open, is given by  $m_{Ca}^2$ . The time evolution of this single-channel open probability follows a Hodgkin-Huxley type model. The steady-state value  $m_{Ca}^\infty$ , as determined according to [87], fits the Boltzmann function to the whole-cell current of an N-type channel. The variable  $m_{Ca}$  approaches its asymptotic value  $m_{Ca}^\infty$  with a time constant  $\tau_{m_{Ca}}$  expressed by means of an ordinary differential equation as

$$\frac{dm_{Ca}}{dt} = \frac{(m_{Ca}^\infty - m_{Ca})}{\tau_{m_{Ca}}}. \quad (13)$$

Additional mathematical expressions for the parameters utilized in (10) are given by

$$I_{PM,Ca} = v_{PM,Ca} \frac{c_i^2}{c_i^2 + K_{PM,Ca}^2}, \quad (14)$$

$$J_{PM,leak} = v_{leak}(c_{ext} - c_i), \quad (15)$$

$$m_{Ca}^\infty = \frac{1}{1 + \exp((V_{m_{Ca}} - V_m)/k_{m_{Ca}})}, \quad (16)$$

where  $v_{PMCa}$  denotes the maximum plasma membrane  $Ca^{2+}$  ATPase (PMCa) current density, determined through computer simulation, so that  $c_i$  is maintained at its resting concentration. The second component of bouton  $Ca^{2+}$ , denoted as  $c_{slow}$ , is recognized for its essential role in short-term plasticity [51]. The release of  $Ca^{2+}$  from the ER is primarily regulated by two types of receptors or  $Ca^{2+}$  channels: the  $IP_3$  receptor and the ryanodine receptor [159]. In this context, the flow is considered to occur solely through the  $IP_3$  receptor. The  $IP_3$  required for the release of  $Ca^{2+}$  from the ER is generated when Glu binds to metabotropic Glu-receptors, activating a G-protein-linked pathway to phospholipase C, which then cleaves phosphatidylinositol (4,5)-bisphosphate ( $PIP_2$ ) to produce  $IP_3$  and diacylglycerol. For modeling this slower  $Ca^{2+}$  signaling process, an adapted Li-Rinzel model is employed (*cf.* [171]). Originally, the model assumes the total intracellular concentration  $c_0$ , is conserved and determines the ER  $Ca^{2+}$  concentration,  $c_{ER}$ , following the relation

$$c_{ER} = \frac{c_0 - c_i}{c_1}. \quad (17)$$

Due to the presence of membrane fluxes, specifically  $I_{Ca}$  and  $I_{PMCa}$ , the assumptions from the original Li-Rinzel model are not applicable in the current model. Moreover, the Li-Rinzel model also incorporates intracellular  $IP_3$  concentration as a control parameter.

To address these discrepancies, two additional equations governing the ER concentrations  $[Ca^{2+}]$  and  $[IP_3]$  have been incorporated into the Li-Rinzel model. The  $IP_3$  production term has been made dependent on Glu to examine the effect of astrocytes  $Ca^{2+}$  on  $c_i$  (cf. [127]). The mathematical model governing the  $c_{slow}$  dynamics is thus given by

$$\frac{dc_{slow}}{dt} = -J_{chan} - J_{ER,pump} - J_{ER,leak}, \quad (18)$$

$$\frac{dc_{ER}}{dt} = -\frac{1}{c_1} \frac{dc_{slow}}{dt}, \quad (19)$$

$$\frac{dp}{dt} = v_g \frac{g_a^{0.3}}{k_g^{0.3} + g_a^{0.3}} - \tau_p(p - p_0), \quad (20)$$

$$\frac{dq}{dt} = \alpha_q(1 - q) - \beta_q q. \quad (21)$$

Here,  $J_{chan}$  represents the  $Ca^{2+}$  flux from the ER to the intracellular space through  $IP_3$  receptors, while  $J_{ER,pump}$  denotes the  $Ca^{2+}$  flux being pumped from the intracellular space back into the ER. The variable  $c_{ER}$  indicates the ER  $Ca^{2+}$  concentration,  $c_1$  is the ratio of ER volume to bouton volume,  $p$  represents the intracellular  $IP_3$  concentration,  $g_a$  signifies the Glu in the extra-SMCs, and  $q$  denotes the fraction of activated  $IP_3$  receptors. These fluxes are described by the following expressions:

$$J_{chan} = c_1 v_1 m_\infty^3 n_\infty^3 q^3 (c_i - c_{ER}), \quad (22)$$

$$J_{ER,pump} = \frac{v_3 c_i^2}{k_3^2 + c_i^2}, \quad (23)$$

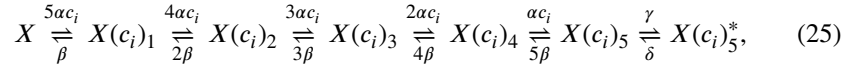
$$J_{ER,leak} = c_1 v_2 (c_i - c_{ER}), \quad (24)$$

with  $m_\infty = \frac{p}{p+d_1}$ ,  $n_\infty = \frac{c_i}{c_i+d_5}$ ,  $\alpha_q = a_2 d_2 \frac{p+d_1}{p+d_3}$  and  $\beta_q = a_2 c_i$ . The values of  $v_1$ ,  $v_2$ , and  $v_3$  are iteratively determined to ensure that  $Ca^{2+}$  homeostasis is maintained within the cell and its organelles.

### 3.2.2 Glu- and GABA-Neuron Dynamics in the Bouton and Smooth Muscle Cell

The dynamics of Glu-neuron interactions are analogous to those observed for GABA-neurons interactions, where Glu has an excitatory effect and GABA is an inhibitor [139]. In the following sections, the mathematical model will be presented, focusing on the Glu-neurons system and its dynamics within the SMCs and the extra-SMCs. In the quadripartite synapse model, both Glu and GABA are incorporated, each with distinct kinetic constants. Glu release within the SMCs is represented as a two-step process:  $Ca^{2+}$  binding to a synaptic vesicle sensor is described according to [17], while synaptic vesicle fusion and recycling follow the framework outlined in [171]. The elevation of extra-synaptic Glu is also approached as a two-step process: the probability of synaptic-like micro-vesicle release is fitted using a modified model of [12], and synaptic-like micro-vesicle fusion and recycling are again modeled following the Tsodyks-Markram model [171], incorporating recent empirical data from [114].

The action potential waveforms result in a temporary rise in intracellular  $[\text{Ca}^{2+}]$ , which subsequently triggers neurotransmitter release [17, 174]. Investigating the sensitivity of  $\text{Ca}^{2+}$  sensors is challenging due to the small size of nerve terminals [174]. It is generally assumed that a  $\text{Ca}^{2+}$  concentration of at least  $100 \mu\text{M}$  is required to activate a *low-affinity*  $\text{Ca}^{2+}$  sensor [126]. However, recent studies conducted in the giant calyx of Held terminal have demonstrated that an intracellular  $\text{Ca}^{2+}$  concentration of approximately  $10 \mu\text{M}$  is sufficient for Glu release [17]. The kinetic model describing  $\text{Ca}^{2+}$  binding to the  $\text{Ca}^{2+}$  sensor is expressed by



where the constants  $\alpha$  and  $\beta$  represent the  $\text{Ca}^{2+}$  association and dissociation rates, respectively, while  $\gamma$  and  $\delta$  are  $\text{Ca}^{2+}$ -independent isomerization constants. The variable  $X$  denotes the  $\text{Ca}^{2+}$  sensor of a synaptic vesicle without any bound  $\text{Ca}^{2+}$  ions, with the index number indicating the number of bound  $\text{Ca}^{2+}$  ions. The isomer  $X(c_i)_5^*$  is the form of  $X(c_i)_5$  that is prepared for Glu release. The fraction of docked vesicles ready for release,  $f_r$ , has been determined using dynamic Monte Carlo simulations [54] based on the kinetics described in (25), which depends on the state  $X(c_i)_5^*$ . This approach is necessary because the number of synaptic vesicles with five  $\text{Ca}^{2+}$  ions bound cannot be estimated by the average vesicle pool due to the limited number of vesicles. The release of neurotransmitters spontaneously depends on the pre-synaptic  $\text{Ca}^{2+}$  concentration [17, 51]. The number of vesicles ready for spontaneous release,  $p_r$ , is assumed to follow a Poisson process [128], which is given by the rate

$$\lambda(c_i) = a_3 \frac{1}{\left(1 + \exp\left(\frac{a_1 - c_i}{a_2}\right)\right)}, \quad (26)$$

that is iteratively adjusted to align with the frequency of spontaneous vesicle release in the presence of an astrocytes, typically ranging from 1 to 3 events per second [93]. The vesicle fusion and recycling process is described by the Tsodyks-Markram model [171]. To incorporate the dependency on  $p_r$ , a slight modification has been made to the Tsodyks-Markram model, yielding

$$\frac{dR}{dt} = \frac{I}{\tau_{rec}} - f_r R, \quad (27)$$

$$\frac{dE}{dt} = -\frac{E}{\tau_{intact}} + f_r R, \quad (28)$$

$$I = 1 - R - E. \quad (29)$$

Here,  $R$  represents the fraction of releasable vesicles within the bouton,  $E$  denotes the fraction of effective vesicles in the SMCs, and  $I$  signifies the fraction of inactive vesicles undergoing recycling. The variable  $f_r$  can take values of 0, 0.5, or 1, corresponding to the number of vesicles ready for release, which are according to 0, 1, or 2. These values are determined either by the stochastic simulation of the kinetic model in (25) or by generating a Poisson random variable with the rate given by (26). The time constants

for vesicle inactivation and recovery are denoted by  $\tau_{inact}$  and  $\tau_{rec}$ , respectively. Once a vesicle is released, the vesicle release process remains inactive for a duration of 6,34 ms in case of Glu and in case of GABA 7,2 ms [43].

Using Monte Carlo simulations of a central glutamatergic synapse, Franks et al. [63] demonstrated that glutamatergic signaling is spatially independent at these synapses. The Glu concentration within a bouton vesicle has been estimated to be 60 mM [37]. Given that  $E$  represents the effective fraction of vesicles in the SMCs, the Glu concentration in the SMCs can be mathematically expressed as

$$\frac{dg}{dt} = n_v g_v E - g_c g, \quad (30)$$

where  $g$  represents the Glu concentration in the SMCs,  $n_v$  is the number of docked vesicles,  $g_v$  denotes the vesicular Glu concentration, and  $g_c$  is the rate of Glu clearance [42]. Using this straightforward dynamic model, it is possible to estimate a range for the Glu concentration in the SMCs from 0.24 to 11 nM [37, 63], as well as to capture the time course of Glu in the SMCs over approximately 2 ms [63, 32]. The governing Glu dynamics in the extra-SMCs is described by

$$\frac{dg_a}{dt} = n_a^v g_a^v E_a - g_a^c g_a, \quad (31)$$

where  $g_a$  is the Glu concentration in the extra-SMCs,  $n_a^v$  represents the readily releasable pool of synaptic-like micro-vesicles,  $g_a^v$  is the Glu concentration within each synaptic-like micro-vesicle and  $g_a^c$  is the clearance rate of Glu from the SMCs due to diffusion and/or re-uptake by astrocytes. Furthermore, it is evident that the formula is similar to Equation (30). In this case, Glu acts on extra-synaptic metabotropic Glu receptors located on the pre-synaptic bouton. This input is used for the  $IP_3$  production term in Equation (18). Unlike the densely packed synaptic vesicles of neurons, the synaptic-like micro-vesicles of astrocytes are less densely packed [13]. Therefore, it is assumed that each synaptic-like micro-vesicle contains 60 mM of Glu and 20 mM of GABA [120].

### 3.2.3 Astrocyte Calcium Dynamics and Gliotransmitter Release

The modulation of astrocytic  $Ca^{2+}$  levels by Glu is described using an astrocytes-specific G-ChI model (*cf.* [40]). This model is referred to as the G-ChI model, based on the dependent variables and the Glu concentration parameter utilized. Within this framework,  $G$  signifies the Glu concentration in the SMCs,  $C$  is the astrocytic  $[Ca^{2+}]$ ,  $h$  represents the gating variable of  $IP_3$  receptors, and  $I$  indicates astrocytic  $IP_3$  concentration. The variable  $g$  is treated as a dynamic variable as described in (30). Within this model, the astrocytic  $Ca^{2+}$  concentration,  $c_a$ , primarily depends on two parameters: the flux from the ER into the cytosol and the maximum pumping capacity of the saroplasmatic reticulum ATPase pump. It is established that  $IP_3$  receptors are organized in clusters within astrocytes [82]. The cluster size,  $N_{IP_3}$ , is not precisely known and is assumed to be 20 in this context (*cf.* [157]). The stochastic Li-Rinzel model is employed here (*cf.* [157]),

which is expressed as

$$\frac{dc_a}{dt} = (r_{Ca} m_\infty^3 n_\infty^3 h_a^3)(c_0 - (1 + c_{1,a})c_a) - v_{ER} \frac{c_a^2}{c_a^2 + K_{ER}^2} + r_L(c_0 - (1 + c_{1,a})c_a), \quad (32)$$

$$\frac{dp_a}{dt} = v_\beta \text{Hill}\left(g^{0.9}, K_R \left(1 + \frac{K_p}{K_R} \text{Hill}(C, K_\pi)\right)\right) + \frac{v_\delta}{1 + \frac{p_a}{k_\delta}} \text{Hill}(c_a^2, K_{PLC\delta}) - v_{3K} \text{Hill}(c_a^4, K_D) \text{Hill}(p_a, K_3) - r_{5p_a} p_a, \quad (33)$$

$$\frac{dh_a}{dt} = \alpha_{h_a}(1 - h_a) - \beta_{h_a} h_a + G_h(t). \quad (34)$$

Equation (32) consists of three terms on the right-hand side. The first one represents the  $\text{Ca}^{2+}$  flux from the ER into the intracellular space with  $r_{Ca}$  denoting the maximal rate of the  $\text{Ca}^{2+}$  flux from the  $\text{IP}_3$  receptor, and  $m_\infty^3 n_\infty^3 h_a^3$  together represent the opening probability of the  $\text{IP}_3$  receptor cluster. The second term describes the rate at which  $\text{Ca}^{2+}$  is removed from the intracellular space by the saroplasmatic reticulum ATPase pump with  $v_{ER}$  representing the maximal rate of  $\text{Ca}^{2+}$ . The third term accounts for the leakage of  $\text{Ca}^{2+}$  from the ER into the intracellular space. Here,  $r_L$  is the maximal rate of  $\text{Ca}^{2+}$  leak from the ER. The terms involved depict similarity to the production terms of  $c_{slow}$  in (18), with the main distinction being that this model operates under a closed-cell assumption. Given this, an expression like (17) holds and can be represented using the astrocytic parameters as

$$c_{ER,a} = \frac{(c_0 - c_a)}{c_{1,a}}, \quad (35)$$

which has the advantage that the astrocytic  $\text{Ca}^{2+}$  flux terms can be represented completely in terms of cell parameters. The second equation (33) consists of four terms on the right-hand side. The first two terms represent the agonist-dependent and agonist-independent production of  $\text{IP}_3$  and the last two incorporate the  $\text{IP}_3$  degradation by  $\text{IP}_3$ -3K and  $\text{IP}_3$ -5P, respectively. In the last equation (34),  $\alpha_{h_a}$  and  $\beta_{h_a}$  denote the rates at which  $h_a$  opens and closes, respectively, and  $G_h(t)$  is a zero mean, uncorrelated, Gaussian white-noise term with a covariance function (*cf.* [157]), given by

$$\langle G_h(t), G_h(t') \rangle = \frac{\alpha_{h_a}(1 - h_a) + \beta_{h_a} h_a}{N_{IP_3}} \delta(t - t'), \quad (36)$$

where  $\delta(t)$  is the Dirac-delta function,  $t$  and  $t'$  are distinct times and the fraction denotes the spectral density (*cf.* [33]). For astrocytic  $\text{Ca}^{2+}$  oscillations, a model incorporating both amplitude and frequency modulation is used, as the coupling between  $\text{IP}_3$  metabolism and CICR does not support amplitude-only modulation [40]. The remaining

expressions used in the equations (32) to (34) are

$$\begin{aligned}
 m_{\infty,a} &= \text{Hill}(p_a, d_1), \\
 n_{\infty,a} &= \text{Hill}(c_a, d_5), \\
 \text{Hill}(x^n, K) &= \frac{x^n}{x^n + K^n}, \\
 \alpha_{h_a} &= a_2 d_2 \frac{p_a + d_1}{p_a + d_3}, \\
 \beta_{h_a} &= a_2 c_a,
 \end{aligned} \tag{37}$$

where the generic Hill function  $\text{Hill}(x^n, K)$  is used for reactions, whose reaction velocity curve is not hyperbolic [96]. Various studies have shown that astrocytes release gliotransmitters in a  $\text{Ca}^{2+}$ -dependent manner [55, 120]. The released gliotransmitters modulate synaptic plasticity through extra-synaptic NMDA receptors [134, 135] and extra-synaptic metabotropic Glu-receptors [138]. The release mechanism of gliotransmitters from astrocytes, similar to that of neurons, occurs in a vesicular manner [120, 13]. Studies indicate that the  $\text{Ca}^{2+}$  dependence of Glu release from hippocampal astrocytes and found that the Hill coefficient for this process ranged between 2.1 and 2.7, indicating that at least two  $\text{Ca}^{2+}$  ions are essential for gliotransmitter release (*cf.* [135]). Consequently, the probability of vesicular fusion in response to mechanical stimulation and the size of the readily releasable pool of synaptic-like micro-vesicles in astrocytes was determined in [114]. Based on the work of Bertram et al. (*cf.* [12]), the model describing gliotransmitter release site activation requires that three  $\text{Ca}^{2+}$  ions must bind to three independent gates or sites ( $S_1 - S_3$ ) to enable gliotransmitter release, which is expressed as

$$C_a + C_j \xrightleftharpoons[k_j^-]{k_j^+} O_j, \quad j \in (1, 2, 3), \tag{38}$$

with  $C_j, O_j$  as the closing and equal opening probabilities of gate  $S_j$ , and,  $k_j^+, k_j^-$ , as the opening and closing rates of the gate  $S_j$ , respectively. The temporal evolution of the open gate  $O_j$  can be expressed as

$$\frac{dO_j}{dt} = k_j^+ c_a - (k_j^+ c_a + k_j^-) O_j. \tag{39}$$

The fraction of synaptic-like micro-vesicles,  $f_r^a$ , ready to be released is described by the product of the opening probabilities,  $O_j$  with  $j \in (1, 2, 3)$ , of the three sites due to their physical independency. The dissociation constants of gates  $S_1, S_2, S_3$  are 108 nM, 400 nM and 800 nM. The time constants for gate closure,  $1/k_j^-$ , are 2,5 s, 1 s and 100 ms.  $S_1$  and  $S_2$ , as well as the time constants, are adapted from [12], while the dissociation and time constant for gate  $S_3$  is determined iteratively to match the experimental data from [114]. When the synaptic-like micro-vesicle is ready to be released, the fusion and

recycling process is modeled by the Tsodyks-Markram model [171], given by

$$\begin{aligned}\frac{dR_a}{dt} &= \frac{I_a}{\tau_{rec}^a} - \Theta(c_a - c_a^{thresh})f_r^a R_a, \\ \frac{dE_a}{dt} &= -\frac{E_a}{\tau_{inact}^a} + \Theta(c_a - c_a^{thresh})f_r^a R_a, \\ I_a &= 1 - R_a - E_a.\end{aligned}\tag{40}$$

In this context,  $R_a$  denotes the fraction of readily releasable synaptic-like micro-vesicles within the astrocytes,  $E_a$  represents the fraction of effective synaptic-like micro-vesicles in the extra-SMCs, and  $I_a$  signifies the fraction of inactive synaptic-like micro-vesicles undergoing endocytosis or re-acidification. The term  $\Theta$  is the Heaviside function, and  $c_a^{thresh}$  represents the threshold of astrocytes  $[Ca^{2+}]$  required for activation of the release site [135]. The time constants for the inactivation and recovery of synaptic-like micro-vesicles are denoted by  $\tau_{inact}^a$  and  $\tau_{rec}^a$ , respectively.

### 3.3 Components of the Neurovascular Coupling Model

To extend the quadripartite synapse model into a NGVU model, it is essential to incorporate smooth muscle and endothelial cell contraction, as well as vascular mechanisms, to achieve completeness. For this purpose, we employ the neurovascular coupling model developed in [45], with necessary modifications to address certain limitations in the original. For instance, the original model incorrectly assumes that astrocytes exhibit action potentials, which is not supported by current understanding. Additionally, it considers potassium as the primary driving component in neurons and astrocytes, an assumption that has been updated in light of recent findings [20]. The neurovascular unit model described in [45] comprises seven fundamental compartments: neurons, the synaptic cleft, astrocytes, the perivascular space, SMCs, ECs, and the arteriolar lumen. These compartments are interconnected through four subsystems: (1) the neuron/astrocyte subsystem, which includes the perivascular space and the synaptic cleft, (2) the smooth muscle cell/endothelial cell subsystem that couples these two cell types, (3) the arteriolar contraction subsystem, and (4) the arteriolar wall mechanical subsystem. The subsystems are modeled as having a triggering input and a subsequent output, which establishes connectivity and serves as a triggering input for other interconnected subsystems [45]. Given the incorrect assumptions about the neuron/astrocyte subsystem in the original model, we include only the latter three subsystems in the NGVU model.

#### 3.3.1 Smooth Muscle and Endothelial Cell Dynamics

The subsystem combining the smooth muscle cell and endothelial cell is based on the work in [100]. In the original model of [45], a KIR channel at the interface between the smooth muscle cell and the perivascular space is included. The inputs for this subsystem are the KIR channel on the smooth muscle cell facing the perivascular space, which allows a flux of  $K^+$  into the cytosol, and the influx of  $IP_3$  into the endothelial cell mediated by luminal agonist P2Y receptors on the endothelial cell membrane [45].

The biochemical behavior of the KIR channel is modeled and implemented based on experimental data from [58] as

$$J_{KIR_i} = \frac{F_{KIR_i} g_{KIR_i}}{\gamma_i} (v_i - v_{KIR_i}), \quad (41)$$

where the conversion parameter  $\gamma_i$  is used to provide  $J_{KIR_i}$  in the correct units of  $\text{mV s}^{-1}$ . The Nernst potential (in mV) is a function of  $K_p$  and is expressed as

$$v_{KIR_i} = z_1 K_p - z_2, \quad (42)$$

where  $z_1$  and  $z_2$  are derived by fitting a linear function according to [58]. The conductance of the KIR channel depends on both the membrane potential  $v_i$  and  $K_p$ . The values of the constants are likewise based on the experimental data from [58]. The second input to the smooth muscle cell/endothelial cell subsystem is the generation of  $\text{IP}_3$  in the endothelial cell due to the activation of membrane receptors by agonists in the arteriolar lumen.  $\text{IP}_3$  mediates the  $J_{IP_3}$  channel in both the endothelial cell and smooth muscle cell, located on the surface of the endothelial cell and saroplasmatic reticulum, allowing  $\text{Ca}^{2+}$  to be released from the reticulum. For a given  $\text{IP}_3$  concentration in the smooth muscle cell/endothelial cell subsystem,  $\text{Ca}^{2+}$  fluctuations can occur due to the CICR process [71, 99]. The production of  $\text{IP}_3$  in endothelial cell is represented by the flux  $J_{EC,IP_3}$ . In this study,  $\text{IP}_3$  production is constant but can be extended to a time-dependent function.

Physiologically, endothelial and SMCs are connected by hetero- and homocellular gap junctions that allow intercellular exchange of molecules and voltage. In the neurovascular unit model in [45], the endothelial and SMCs are modeled as a single subsystem, thus the homocellular exchange between cells is neglected. The linearized coupling functions for the heterocellular exchange of calcium, voltage, and  $\text{IP}_3$  are given by

$$J_{Ca^{2+}_{cpt}} = -P_{Ca^{2+}} ([Ca^{2+}]_i - [Ca^{2+}]_j), \quad (43)$$

$$J_{V_{cpt}} = -G_v (V_i - V_j), \quad (44)$$

$$J_{IP_3,cpt} = -P_{IP_3} ([IP_3]_i - [IP_3]_j), \quad (45)$$

where the subscripts  $i$  and  $j$  correspond to endothelial and SMCs, respectively. Additionally, calcium buffering is incorporated to account for the fact that approximately 1% of the intracellular  $\text{Ca}^{2+}$  is free [136].

### 3.3.2 Arteriolar Contraction Model

The contraction force is generated through the formation of cross-bridges between actin and myosin filaments, a process regulated by cytosolic  $\text{Ca}^{2+}$ . The model for the arteriolar contraction subsystem builds upon the foundational work of Hai and Murphy [73]. The input signal for this model is the compartmental cytosolic  $\text{Ca}^{2+}$  concentration in SMCs. Myosin exists in four potential states during this process: free non-phosphorylated cross-bridges (M), free phosphorylated cross-bridges (Mp), attached phosphorylated cross-bridges (AMp), and attached dephosphorylated latch-bridges (AM). The dynamics of

the fraction of myosin in each state are described by the following four equations as

$$\frac{d[MP]}{dt} = K_4[AMP] + K_1[M] - (K_2 + K_3)[MP], \quad (46)$$

$$\frac{d[AMP]}{dt} = K_3[MP] + K_6[AM] - (K_4 + K_5)[AMP], \quad (47)$$

$$\frac{d[AM]}{dt} = K_5[AMP] - (K_7 + K_6)[AM], \quad (48)$$

$$[M] = 1 - [AM] - [AMP] - [MP], \quad (49)$$

where the rate constants  $K_n$  with  $n = (1, \dots, 7)$  control the phosphorylation and bridge formation processes. The  $\text{Ca}^{2+}$  dependence of the cross-bridge model is governed by the rate constants  $K_1$  and  $K_6$ . According to [100], the total phosphorylation of myosin is a function of the smooth muscle cell compartmental  $\text{Ca}^{2+}$ . Thus,  $K_1$  and  $K_6$  are defined by the constants characterizing the  $\text{Ca}^{2+}$  sensitivity of calcium-activated phosphorylation of myosin as

$$K_1 = K_6 = \gamma_{cross} [\text{Ca}^{2+}]_i^3. \quad (50)$$

The active stress in a smooth muscle cell is directly proportional to the fraction of attached cross-bridges,  $F_r$ , which serves as an input parameter for the mechanical subsystem. The fraction of attached cross-bridges is mathematically described as follows

$$F_r = \frac{[AMP] + [AM]}{([AMP] + [AM])_{max}}. \quad (51)$$

$([AMP] + [AM])_{max}$  represents the maximum possible value of the sum of the concentrations of attached phosphorylated ( $[AMP]$ ) and dephosphorylated ( $[AM]$ ) cross-bridges. It is used for normalization, ensuring that  $F_r$  is dimensionless and scaled between 0 and 1, which facilitates its use as an input parameter for the mechanical subsystem.

### 3.3.3 Visco-Elastic Model of the Arteriolar Wall

The mechanical properties of the arterial wall are assumed as visco-elastic and are modeled following the Kelvin-Voigt approach. This model comprises a Newtonian damper and a Hookean elastic spring connected in parallel. The input signal, which corresponds to the active stress state of the smooth muscle cell in the circumferential direction, is the fraction of attached myosin cross-bridges,  $F_r$ , from the mechanical subsystem. The circumferential stress in the arterial wall,  $\sigma_{\theta\theta}$ , is given by the linear elastic part with the Young's modulus  $E$ , and the viscous part with the viscosity  $\eta$ , as

$$\sigma_{\theta\theta} = E\epsilon_{\theta\theta} + \eta \frac{d\epsilon_{\theta\theta}}{dt} = \frac{R\Delta p}{h}, \quad (52)$$

where  $\epsilon_{\theta\theta}$  is the strain in the arterial wall,  $\Delta p$  represents the transmural pressure,  $R$  denotes the vessel radius, and  $h$  is the vessel thickness. For simplicity, the wall thickness in this simulation is considered a constant fraction of the radius, with  $h = 0.1R$ . The parameters of this subsystem are adapted from experimental data available in [39]. A

linear function is employed to map the transition from the fully activated state to the fully relaxed state, applicable to radii between  $10\ \mu\text{m}$  and  $30\ \mu\text{m}$ . The Young's modulus as well as the initial radius are assumed to be continuous functions of  $F_r$ , with a linear interpolation between the active ( $E_{act}$ ) and passive ( $E_{pas}$ ) experimental data points provided in [39], expressed as

$$E(F_r) = E_{pas} + F_r(E_{act} - E_{pas}). \quad (53)$$

This approach can similarly be applied to represent the initial radius, yielding

$$R_0(F_r) = R_{0,pas} + F_r(R_{0,act} - R_{0,pas}). \quad (54)$$

Transforming the latter equations into a time-dependent expression for the vessel radius results in

$$\frac{dR}{dt} = \frac{R_{0,pas}}{\eta} \left( \frac{R\Delta p}{h} - E(F_r) \frac{R - R_0(F_r)}{R_0(F_r)} \right). \quad (55)$$

The final equation (55) describes the dynamic behavior of the vessel radius as a function of the transmural pressure, visco-elastic properties of the wall, and the activation state of SMCs via  $F_r$ . This expression expressed the connection between mechanical forces and active stress, allowing for a time-dependent simulation of arteriolar behavior under varying physiological conditions, providing a model for the dynamic regulation of blood flow and vessel radii in response to changes in transmural pressure and smooth muscle activation.

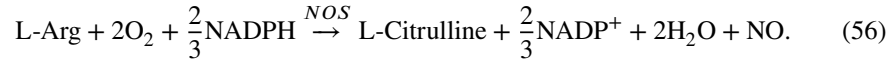
### 3.3.4 Influence of the Nitric Oxide Signaling Pathway

NO plays a fundamental role in neurovascular coupling by mediating the dynamic regulation of vascular tone in response to neuronal activity. As a potent vasodilator, NO is critical for linking cellular signaling processes to changes in arteriolar diameter and cerebral blood flow. Its high diffusivity and involvement in complex biochemical pathways necessitate its inclusion in the neurovascular coupling model to achieve a mechanistic understanding of the connection between neuronal activation, vascular responses, and metabolic demands [44]. The NO signaling pathway model is based on [44], which is an addition to their previously introduced neurovascular unit model (*cf.* [45]). The NO signaling pathway is mathematically described by production, diffusion and consumption terms in different cells, as well as the interaction of NO with other biochemical species and ion channel open probabilities [44].

The production of NO is driven by the two constitutive isoforms of nitric oxide synthases (NOS), neuronal nitric oxide synthases (nNOS) and endothelial nitric oxide synthases (eNOS) [60]. The activation of both enzymes is mediated by intracellular  $\text{Ca}^{2+}$  in the neurons and ECs, respectively. Additionally, eNOS is activated by blood flow-induced wall shear stress in cerebral arterioles [91]. Due to its high diffusion coefficient, NO rapidly diffuses into other compartments, as demonstrated by experimental data [115] and kinetic simulations [105]. When NO reaches the smooth muscle cell, it interacts with intracellular enzymes to regulate smooth muscle cell relaxation [181]. The dynamics of NO in the various compartments are described using mass balance equations. The concentration of NO in each domain is determined by the balance between

production, intracellular consumption, and diffusion to and from other compartments. Fig. 4 graphically illustrates the NO signaling pathway.

The rate of NO production is determined by the concentration of activated NO synthases. The essential biochemical substrates for this process include L-Arginine (L-Arg),  $O_2$ , and nicotinamide adenine dinucleotide phosphate (hydrogen) (NADPH) [27], with L-Arg serving as the crucial nitrogen donor [62]. During the reaction, L-Arg is converted into L-citrulline, producing nicotinamide adenine dinucleotide phosphate (NADP)<sup>+</sup>, water, and NO in the process. This reaction involves a five-electron oxidation that occurs in two distinct steps, and the overall stoichiometric equation is given by



Several biomolecule cofactors, including flavin mononucleotide, flavin adenine dinucleotide, and tetrahydrobiopterin, are required for the reaction. The constitutive NOS isoforms, nNOS and eNOS, are considered the primary producers of NO and play a crucial role in maintaining homeostasis [60]. Consequently, in this model, NO production is limited to neurons and ECs, with the production rates in astrocytes ( $p_{NO,k}$ ) and SMCs ( $p_{NO,i}$ ) set to zero. In neurons, the synthesis of NO is catalyzed by nNOS, which is activated in response to glutamate-induced calcium influx into the post-synaptic neurons. The production of NO in neurons depends on the concentration of activated nNOS and is further constrained by the availability of  $O_2$  and L-Arg [27]. This relationship is expressed mathematically through the maximum neuronal production rate,  $p_{max}$ , as

$$p_{NO,n} = p_{max} \frac{[O_2]_n}{K_{m,O_2,n} + [O_2]_n} \frac{[L-Arg]_n}{K_{m,L-Arg,n} + [L-Arg]_n}, \quad (57)$$

$$p_{max} = V_{max,NO,n} [nNOS_{act}]_n.$$

The maximum catalytic rate of nNOS, denoted as  $V_{max,NO,n}$ , along with the neuronal concentrations of  $O_2$  and L-Arg,  $[O_2]_n$  and  $[L-Arg]_n$ , respectively, and the Michaelis constants  $K_{m,O_2,n}$  and  $K_{m,L-Arg,n}$ , define the reaction kinetics (cf. [27]). The activation of nNOS in the neurons is induced by the neurotransmitter Glu in response to neuronal activation. In a chemical synapse, when an action potential arrives at the presynaptic neuronal axon terminal, Glu is released from vesicles into the synaptic cleft. This Glu then binds to receptors on the dendrite of the postsynaptic neurons and is subsequently cleared from the synaptic cleft through diffusion and hydrolysis (cf. [44, 20, 164]), as described in the quadripartite synapse model in Section 3.2.2.

Since the neuronal NOS is often co-localized with ionotropic NMDA-receptors [118, 61], which are receptor complexes including transmembrane ion channels in the neurons that are opened or closed in response to the binding of Glu [10]. There are two different types of NMDA-receptors, NR2A and NR2B, which show different opening probabilities,  $w$ , which depend on the neuronal Glu concentration using Michaelis-Menten kinetics to meet the experimental data from [149]. Mathematically, the opening probability  $w$  is described by

$$w_{NR2,i} = \frac{[Glu]_{sc}}{K_{m,i} + [Glu]_{sc}}, \quad i \in \{A, B\}, \quad (58)$$

where  $K_{m,A}$  and  $K_{m,B}$  are the fitted Michaelis constants. Given that NMDA receptors are highly permeable to  $\text{Ca}^{2+}$  ions (*cf.* [89]), the glutamate-induced  $\text{Ca}^{2+}$  flux is incorporated into the model. The total calcium current,  $I_{Ca,tot}$ , is expressed as

$$\begin{aligned} I_{Ca,tot} &= I_{Ca}(0.63w_{NR2,A} + 11w_{NR2,B}) \\ I_{Ca} &= \frac{4v_n G_M (P_{Ca}/P_M) ([Ca^{2+}]_{ex}/[M]) \exp(2v_n F/(R_{gas} T))}{1 + \exp(\alpha_v(v_n + \beta_n))} \frac{\exp(2v_n F/(R_{gas} T))}{1 - \exp(2v_n F/(R_{gas} T))}, \end{aligned} \quad (59)$$

where  $I_{Ca}$  is the neuronal inward calcium current,  $F$  is Faraday's constant,  $v_n$  is the neuronal membrane potential,  $G_M$  is the conductance, and  $P_{Ca}/P_M$  is the ratio of NMDA receptor permeabilities to  $\text{Ca}^{2+}$  and monovalent ions. Additionally, the model accounts for the external calcium concentration  $[Ca^{2+}]_{ex}$ , the concentration of monovalent ions  $[M]$ , and the intra- and extracellular translation factors  $\alpha_v$  and  $\beta_v$ . The temperature  $T$  and the universal gas constant  $R_{gas}$  are also included. The estimated arrival of 0.63 NR2A- and 11 NR2B-NMDA-receptors, on average per synapse, is based on measurements from [149]. In the endothelial cell, NO production is facilitated by the constitutive enzyme isoform eNOS, whose catalytic activity depends on the availability of  $\text{O}_2$  and L-Arg. The endothelial NO production can be described by

$$p_{NO,j} = V_{max,NO,j} [eNOS_{act}]_j \frac{[O_2]_j}{K_{m,O_2,j} + [O_2]_j} \frac{[L - Arg]_j}{K_{m,L-Arg,j} + [L - Arg]_j}. \quad (60)$$

The maximal activity of eNOS is regulated by the intracellular calcium concentration and is further influenced by wall shear stress, which arises from blood flow through the perfusing arteriole. Wall shear stress activates a signaling cascade involving phosphatidylinositol 3-kinase and the serine/threonine-specific protein kinase, which phosphorylates eNOS [27, 35, 44]. The elastic strain energy stored within the vessel membrane, as well as the quantification of exogenous  $\text{Ca}^{2+}$  entry via shear stress-gated ion channels, is detailed in [35]. The strain energy stored in the membrane,  $F_{wss}$ , and the strain energy density,  $W_{wss}$ , are described mathematically in [176]. Wall shear stress,  $\tau_{WSS}$ , represents the frictional force per unit area and establishes a positive feedback mechanism: increased wall shear stress enhances NO production by ECs, inducing vasodilation and further modifying the shear stress. The wall shear stress  $\tau_{WSS}$  in the arteriolar wall depends on the regional CBF,  $Q$ , which is modeled using the Hagen–Poiseuille flow assumption for cerebral arterioles.

The diffusion of NO, denoted as  $d_{NO,m}$ , can be derived from Fick's second law of diffusion, which characterizes the diffusion of a substance over time and space. To simplify the diffusion formulation, the Einstein-Smoluchowski equation is employed, describing the characteristic time required for NO to diffuse a certain distance from the center of one cell to another. The compartment model outlines the diffusion between different domains but does not account for the amount of NO released into the lumen and subsequently scavenged by reactions with hemoglobin. The diffusion term of a linear diffusion

is given by

$$d_{NO,m} = \frac{[NO]_{out} - [NO]_{in}}{\tau_{\Delta x,m}}, \quad m \in \{n, a, s, e\}, \quad (61)$$

$$\tau_{\Delta x,m} = \frac{(\Delta x_m)^2}{2D_{c,NO}}, \quad (62)$$

where  $m \in \{n, a, s, e\}$  denotes the cell indices for neurons, astrocytes, smooth muscle and ECs, respectively,  $\tau_{\Delta x}$  represents the characteristic time required for NO to diffuse over a specific distance  $\Delta x_m$  from the center of one cell to another. For example, the distances between the centers of the neurons and astrocytes is roughly 25  $\mu\text{m}$  [44, 95].

The consumption of NO is denoted as  $c_{NO,m}$ . As a free radical, NO readily reacts with biochemical species containing unpaired electrons, such as molecular  $\text{O}_2$ , superoxide anions, and metals [118]. NO is scavenged in the cytosol of all cell types through which it diffuses. The mathematical expression for the scavenging term across all model compartments is given by:

$$c_{NO,m} = k_m [NO]_m C_m, \quad m \in \{n, a, e\}, \quad (63)$$

where  $C_m$  is the concentration of reactive species in the cell type, and  $k_m$  is the reaction rate constant [95]. In the smooth muscle cell, NO affects the contraction mechanism and the open probability of the large conductance  $\text{Ca}^{2+}$ -dependent  $\text{K}^+$  channel (BK) channel via its second messenger, cGMP. Additionally, NO activates soluble guanylyl cyclase, an enzyme that catalyzes the formation of cGMP. The kinetics of these processes are described in [181].

### 3.4 Integration of Synapse and Vascular Components in NGVU

To integrate the quadripartite synapse and vascularization models into a coherent NGVU model, the interaction points between subsystems must be carefully addressed. First, the neurons/astrocytes subsystem from the original neurovascular unit model in [45] is extended with the quadripartite synapse model, while the vascularization components retain the smooth muscle cell/endothelial cell model, as well as the arteriolar contraction and mechanical wall models. Specifically, the astrocytic  $\text{Ca}^{2+}$  released over time is incorporated into the sarcoplasmic reticulum as an uptake process. The  $\text{Ca}^{2+}$  flux into the sarcoplasmic reticulum is modeled a

$$J_{SR_{uptake,i}} = B_i \frac{[Ca^{2+}]_i^2}{c_{bi}^2 + [Ca^{2+}]_i^2}, \quad (64)$$

where  $[Ca^{2+}]_i$  represents the time-dependent  $\text{Ca}^{2+}$  dynamics in astrocytes as defined by the quadripartite synapse model. The  $\text{Ca}^{2+}$  release through the sarcoplasmic reticulum leak channel is driven by  $\text{IP}_3$  generation. The initial input to the smooth muscle cell/endothelial cell subsystem through the KIR channel is retained in the NGVU model. Fig. 4 provides an overview of the complete NGVU model, integrating the quadripartite synapse and vascularization components, along with the relevant channels and fluxes.

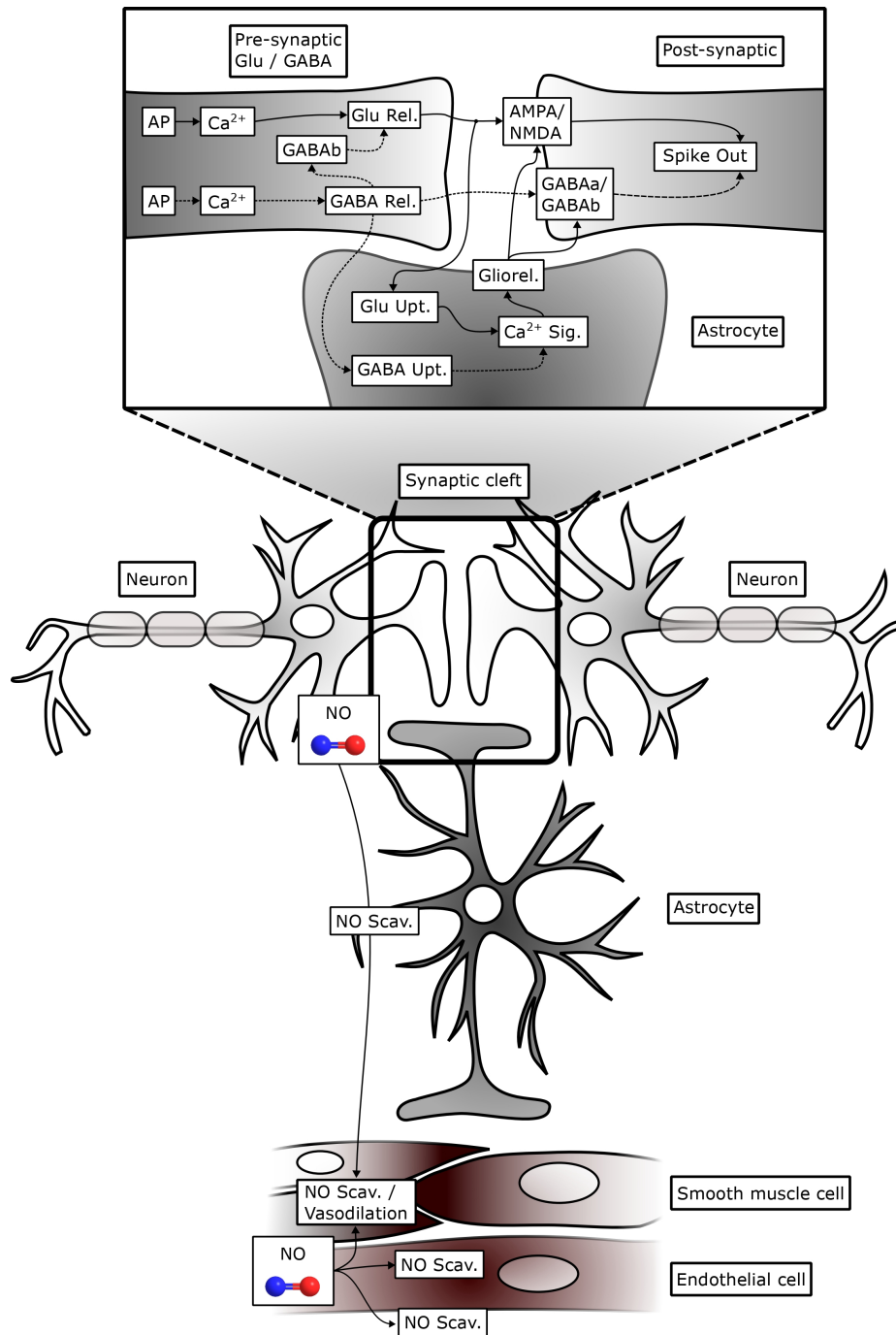


Fig. 4: Components of the NGVU. Quadripartite synapse with pre-synaptic Glu/GABA neurons (top left), post-synaptic neuron (top right), astrocyte (center). Action potentials (AP) lead to  $Ca^{2+}$  influx, triggering Glu Rel./GABA Rel. into the synaptic cleft. The astrocyte uptakes neurotransmitters (Glu Upt., GABA Upt.) and, via  $Ca^{2+}$  Sig., releases gliotransmitters (Gliorel.). Endothelial and SMCs (bottom) regulate vasodilation through NO production and NO scavenging (Scav.). Abbreviations: AMPA/NMDA – excitatory receptors, GABA<sub>A</sub>/GABA<sub>B</sub> – inhibitory receptors, Spike Out – post-synaptic spiking.

To integrate the gasotransmitter NO into the NGVU model, Yang et al. [181] proposed two pathways through which NO can induce local vasodilation of arterioles in the brain. The first pathway involves an indirect influence on the smooth muscle cell contractile system, which is governed by the formation of cross-bridges between actin and myosin filaments, as initially described by Hai and Murphy [72]. Furthermore, cGMP exerts a regulatory effect on the myosin dephosphorylation process, altering the rate constants for dephosphorylation as described by Yang et al. [181], represented by

$$R_{cGMP} = \frac{[cGMP]_i^2}{K_{m,mlcp}^2 + [cGMP]_i^2}, \quad (65)$$

$$K_{2c} = K_{5c} = \delta_i(k_{mlpc,b} + k_{mlpc,c}R_{cGMP}), \quad (66)$$

where  $K_{m,mlcp}$  denotes the Michaelis constant,  $k_{mlpc,b}$  is the basal myosin light-chain dephosphorylation rate constant,  $k_{mlpc,c}$  is the first-order rate constant for cGMP-regulated myosin light-chain dephosphorylation, and  $\delta_i$  is a constant fitted to experimental data (cf. [181, 72]). The second messenger of NO, cGMP, modifies the rate constants for the dephosphorylation of  $Mp$  to  $M$  and  $AMp$  to  $AM$  via myosin light-chain phosphatase [181]. The second pathway concerns the open probability,  $w_i$ , of the BK channel in SMCs, which is a function of the membrane potential,  $v_i$ , and is shifted to the left in the membrane potential space by cGMP (cf. [162]). Instead of using the open probability of the BK channel as described by Koenigsberger et al. [100], the influence of NO is incorporated as a cGMP-dependent modification of the open probability,  $w_i$ . Mathematically, this is expressed as

$$c_{w,i} = \frac{1}{\epsilon_i + \alpha_i \exp(\gamma_i [cGMP]_i)}, \quad (67)$$

where  $\epsilon_i$ ,  $\alpha_i$ , and  $\gamma_i$  are translation factors calibrated to match the observed data from Stockand and Sansom [162]. Furthermore, to fully integrate the NO model into the NGVU model, we use the Glu in the synaptic cleft, provided by the quadripartite synapse model.

## 4 Numerical Simulation Results

The following sections present the computational results of our integrated neuro-glial-vascular coupling model. The findings are organized to provide a detailed examination of the macrocirculation dynamics, neurotransmitter release, neuronal spiking activity, astrocytic signaling, neurovascular responses, and microcirculation within a representative unit of the DVC. Each subsection highlights specific aspects of the modeled system, emphasizing the interactions between neuronal, astrocytic, and vascular components and their implications for blood flow regulation and metabolic support in the DVC. These results validate the framework and provide mechanistic insights into the physiological processes underlying neurovascular coupling. In all subsequent cellular-scale (0D) analyses, the displayed results are exemplary for the capillary vessel that receives the prescribed arterial inflow. As shown schematically in Figure 5, the simulation workflow couples the macrocirculation and neurovascular microcirculation over a single heart-beat period ( $T$ ).

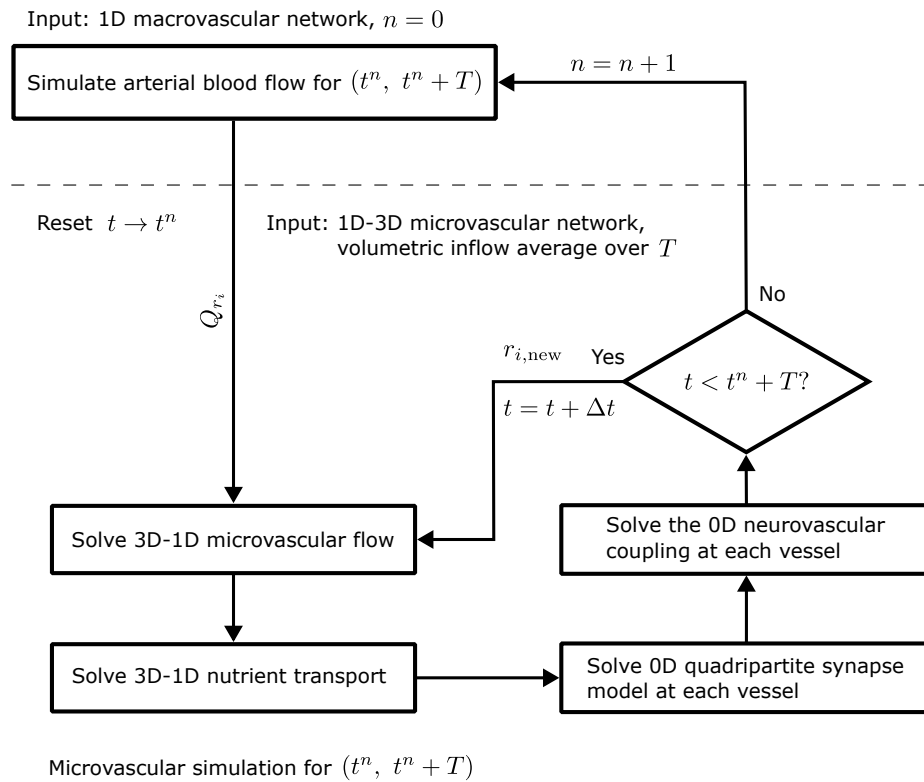


Fig. 5: Schematic of the simulation workflow during one heartbeat period ( $T$ ), illustrating the sequential coupling between the 1D macrovascular network and the neurovascular-coupled 3D-1D-0D microvascular network.

#### 4.1 Macrocirculation Dynamics

Figure 6 depicts the flow and pressure in our 1D-0D coupled model described in Section 3.1.1 at some sample points on the path from the aorta to the vessels that are coupled with the 3D-1D coupled microcirculation model (see Section 3.1.2). The average flows  $Q_0$  used in the coupling are indicated by dotted lines. For the given setting assuming  $\gamma = 3$  we obtain:

$$Q_0 \approx 0.46 \frac{\text{cm}^3}{\text{s}}.$$

Based on this value we have for  $\Lambda_c$  the following inflow rates:

$$Q_{r,c,1} \approx 8.19 \times 10^{-8} \frac{\text{cm}^3}{\text{s}} \text{ and } Q_{r,c,2} \approx 5.75 \times 10^{-8} \frac{\text{cm}^3}{\text{s}}.$$

The pressure curves in our macrovascular network exhibit the typical shape of pressure

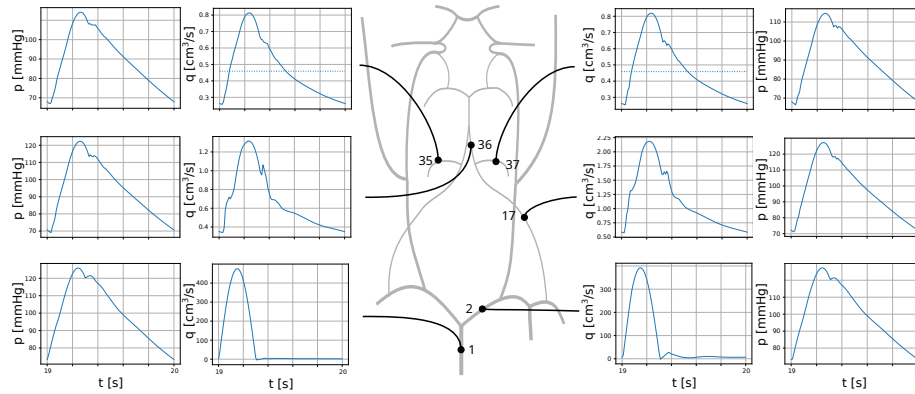


Fig. 6: Flow and pressure in our Circle-of-Willis close to the coupling point with our microcirculation model.

curves in larger arteries. It can be observed that the pressures are within a reasonable range of about 70 mmHg to about 125 mmHg. During the systole we have a strong increase and during the diastole a slow decay is seen. At the interface of both phases there is a characteristic kink caused by the closing of the aortic valve. Due to the Windkessel effect caused by the models attached to the outlets of the macrovascular network the flow rates do not fall back to zero apart from the aorta. This ensures a constant blood supply of the organs linked to the different outlets.

#### 4.2 Neurotransmitter Release and Synaptic Activation

Figure 7 illustrates the dynamics of neurotransmitter release and synaptic activation in a representative 0D quadripartite synapse system associated with a single blood vessel. These results highlight the temporal variations in the concentrations of Glu and GABA

within the nerve terminals and synaptic cleft, which serve as critical inputs to the neuroglial-vascular coupling model.

In the case of glutamate, stored Glu in the nerve terminal (Figure 7a) gradually decreases due to synaptic activation, leading to the release of free Glu within the terminal (Figure 7b). A corresponding increase in glutamate concentration in the synaptic cleft is observed (Figure 7c), representing effective neurotransmitter signaling. Similarly, stored GABA (Figure 7d) transitions into free GABA (Figure 7e) and is subsequently released into the synaptic cleft (Figure 7f). These dynamics reflect the interplay of excitatory (Glu) and inhibitory (GABA) neurotransmitter systems, which are fundamental to maintaining synaptic balance and initiating downstream cellular responses.

In addition to the neurotransmitter dynamics, Figure 8 illustrates the temporal evolution of key signaling molecules, including inositol trisphosphate ( $[IP_3]$ ) and calcium ion ( $[Ca^{2+}]$ ) concentrations. The  $[IP_3]$  dynamics in the glutamate nerve terminal, shown in Figure 8a, and the GABA nerve terminal, shown in Figure 8b, play a critical role in regulating neurotransmitter release and ensuring proper synaptic function. Furthermore, the dynamics of intracellular calcium stores, depicted in Figure 8c and Figure 8d for the ER of glutamate and GABA neurons, respectively, are pivotal for neurotransmitter release and downstream signaling events. These results highlight the intricate cascade of signaling events triggered by synaptic activation, emphasizing the importance of both  $[IP_3]$  and  $[Ca^{2+}]$  in maintaining synaptic activity and influencing neurovascular interactions. Together, these figures emphasize the intricate signaling events within the quadripartite synapse model, which captures the interactions between neurons, astrocytes, and the vascular system. This representative system highlights the local coupling between synaptic activation and vascular responses, contributing to the neuroglial-vascular coupling framework.

### 4.3 Neuronal Spiking Activity

The neuronal spiking activity associated with a representative quadripartite synapse system is shown in Figures 9 and 10. These figures provide an in-depth view of the electrical dynamics and synaptic currents that govern the interaction between excitatory and inhibitory components in the synapse.

Figure 9 illustrates the temporal evolution of action potentials and synaptic currents. Panel (a) depicts the action potential at the Glu presynaptic nerve terminal, characterized by rapid depolarization and repolarization cycles. This reflects the excitation dynamics triggered by Glu neurotransmitter release, essential for synaptic activation and downstream signaling. Panel (b) shows the action potential at the GABA presynaptic nerve terminal, where the amplitude and timing differ from those of the Glu terminal, highlighting the distinct role of inhibitory neurotransmission in modulating the overall synaptic response.

Panel (c) presents the excitatory post-synaptic current (EPSC), which results from the cumulative release of Glu neurotransmitters into the synaptic cleft and their binding to post-synaptic receptors. The EPSC curve demonstrates the temporal summation of excitatory inputs, driving the post-synaptic neuron toward depolarization. In contrast, panel (d) displays the inhibitory post-synaptic current (IPSC), generated by the release

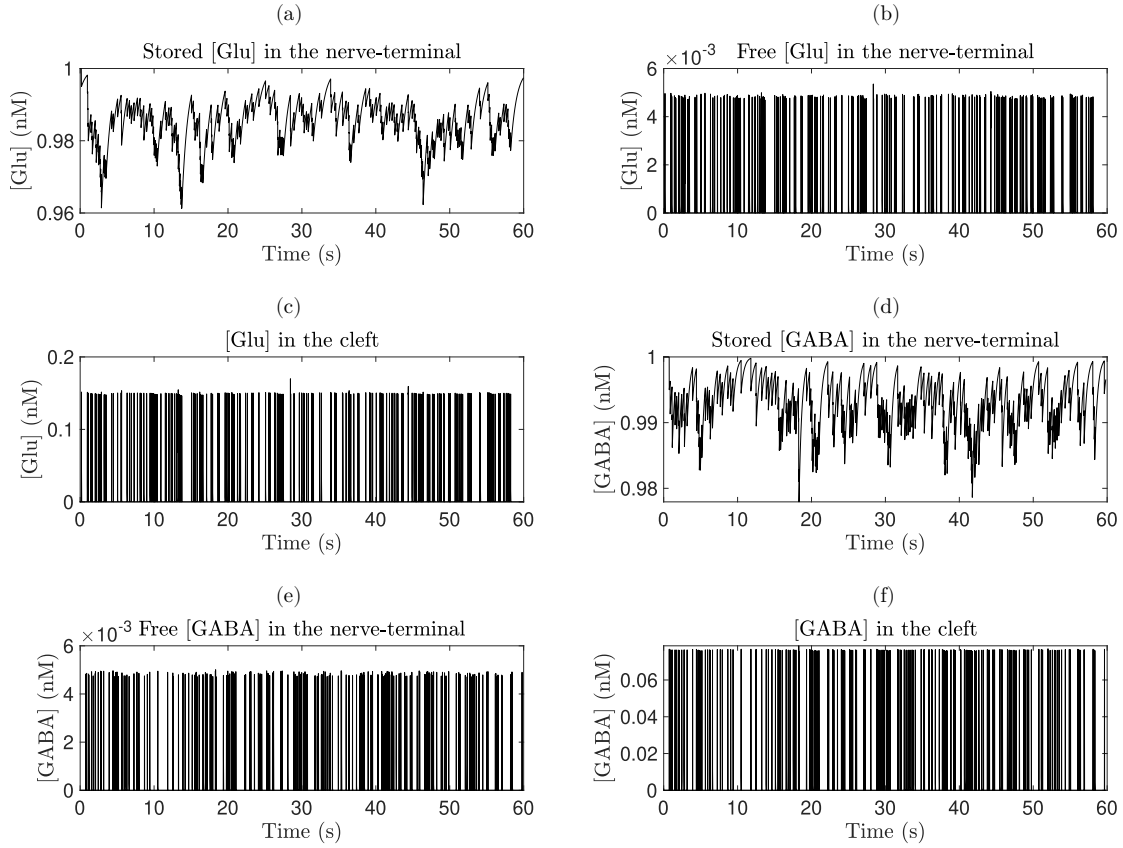


Fig. 7: Dynamics of neurotransmitter release in a representative 0D quadripartite synapse system associated with one vessel. (a) Stored glutamate [Glu] in the nerve terminal, (b) Free glutamate [Glu] in the nerve terminal, (c) Glutamate [Glu] in the synaptic cleft, (d) Stored GABA in the nerve terminal, (e) Free GABA in the nerve terminal, and (f) GABA in the synaptic cleft.

of GABA neurotransmitters. The IPSC curve represents the inhibitory effect on the post-synaptic neuron, counteracting excitatory signals and maintaining neuronal balance.

Figure 10 focuses on the post-synaptic potential (PSP), which integrates the effects of excitatory and inhibitory inputs at the post-synaptic neuron. The PSP curve exhibits the combined depolarization and hyperpolarization phases, illustrating how synaptic inputs modulate the membrane potential and influence the likelihood of action potential generation. The dynamics of the PSP are critical for understanding the interplay between excitation and inhibition in synaptic activity and their implications for downstream neuro-glial interactions.

These results provide a comprehensive overview of neuronal spiking activity and its role in regulating synaptic responses within the quadripartite synapse system. By

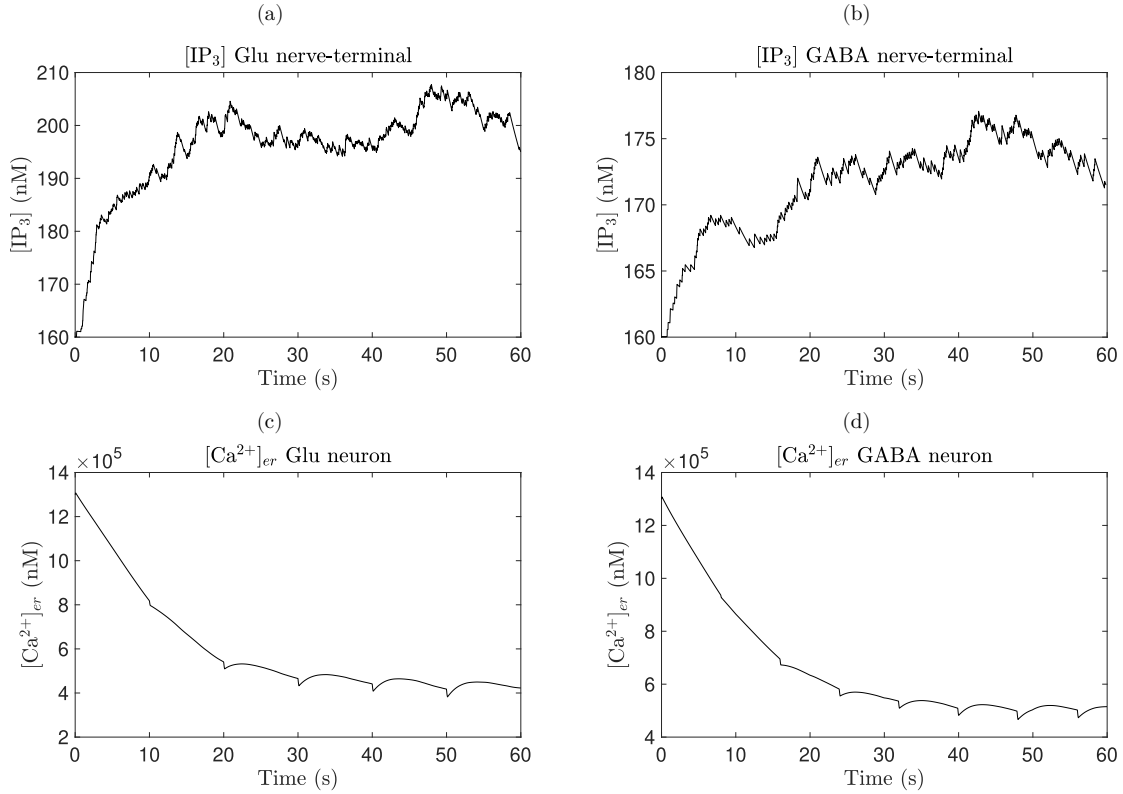


Fig. 8: Dynamics of signaling molecules in the neuro-glial system for a representative quadripartite synapse system. (a) [IP<sub>3</sub>] in the glutamate nerve terminal, (b) [IP<sub>3</sub>] in the GABA nerve terminal, (c) [Ca<sup>2+</sup>]<sub>er</sub> in the ER of the glutamatergic neuron, and (d) [Ca<sup>2+</sup>]<sub>er</sub> in the ER of the GABA neuron.

capturing both excitatory and inhibitory dynamics, this analysis highlights the intricate balance required for effective neurotransmission and sets the stage for further exploration of astrocytic and vascular responses in the neuro-glial-vascular coupling framework.

#### 4.4 Astrocytic Calcium and Gliotransmitter Signaling

Astrocytes serve as pivotal mediators within the NGVU, responding to neuronal activity with intricate Ca<sup>2+</sup> and IP<sub>3</sub> signaling cascades. These signals are not only essential for regulating gliotransmitter release but also play a critical role in vascular responses.

Figure 11 illustrates the temporal evolution of astrocytic [IP<sub>3</sub>] and [Ca<sup>2+</sup>] concentrations. The left panel shows the dynamics of [IP<sub>3</sub>], a key second messenger involved in intracellular calcium release. The rapid increase in [IP<sub>3</sub>] upon neuronal activation triggers calcium release from intracellular stores, as reflected in the right panel. The [Ca<sup>2+</sup>] dynamics exhibit an initial sharp rise followed by a slower decay, characteris-

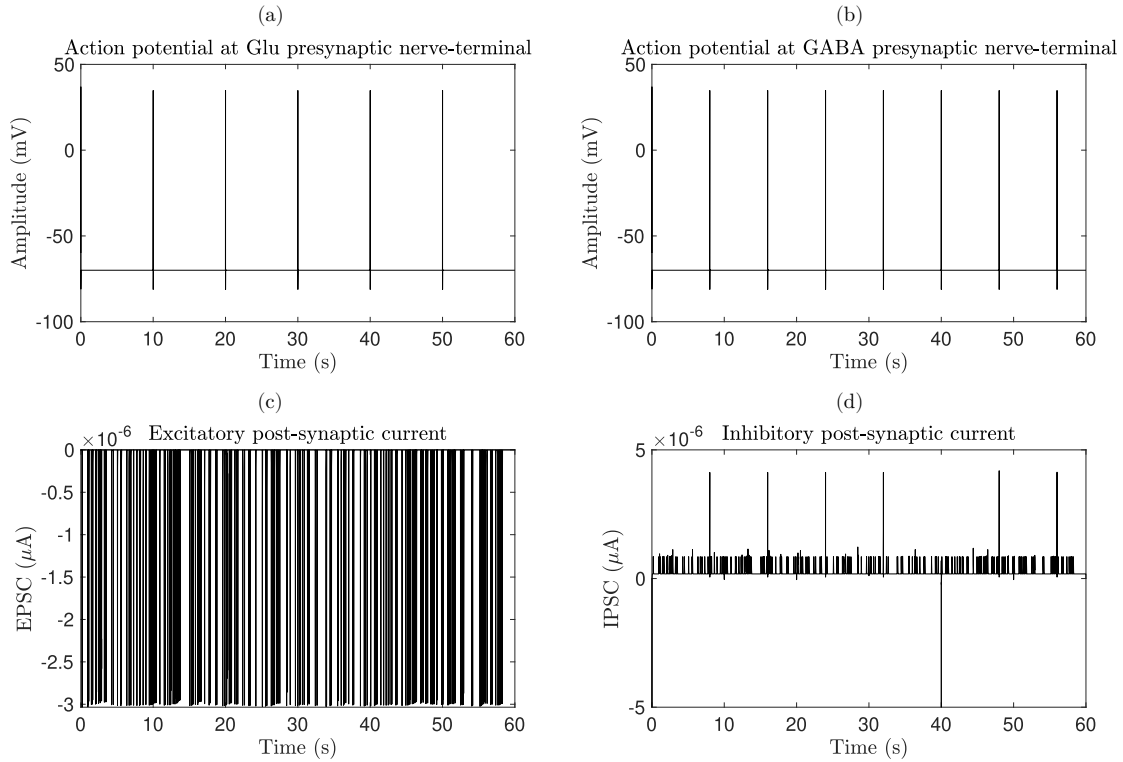


Fig. 9: Neuronal spiking activity and synaptic currents for a representative quadripartite synapse system. (a) Action potential at the glutamatergic presynaptic nerve terminal, (b) Action potential at the GABA presynaptic nerve terminal, (c) EPSC, and (d) IPSC.

tic of astrocytic calcium signaling. This biphasic pattern reflects the interplay between  $[\text{IP}_3]$ -mediated release and cellular mechanisms for calcium sequestration and extrusion.

Astrocytic calcium signaling underpins gliotransmitter release, facilitating crosstalk between neurons and the vascular system. By capturing these dynamics, our model emphasizes the astrocyte's role in neurovascular coupling, where gliotransmitters regulate blood vessel tone and metabolic support for active neurons.

#### 4.5 Neurovascular Response

Figure 12 illustrates the temporal dynamics of calcium and inositol trisphosphate ( $\text{IP}_3$ ) signaling within vascular SMCs and ECs, key components in the neurovascular coupling process. The intracellular calcium concentration in SMCs exhibits oscillatory behavior over time, which is critical for regulating vascular tone. These calcium dynamics mediate vasoconstriction and vasodilation by modulating the contractile state of SMCs, thereby directly influencing the radius of the blood vessel. Similarly, the intracellular calcium signals in ECs play a complementary role by driving the release of vasoactive media-

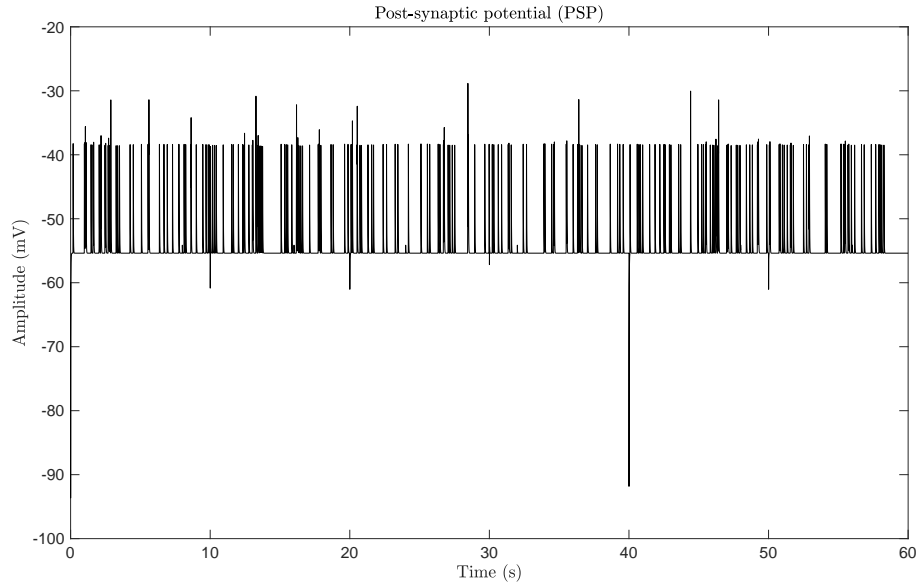


Fig. 10: PSP for a representative quadripartite synapse system. The PSP reflects the combined effects of excitatory and inhibitory inputs.

tors such as NO and prostacyclin. These mediators propagate the effects of endothelial activation to adjacent SMCs, ensuring coordinated vascular responses.

The  $IP_3$  signaling pathways, shown in the same figure, highlight the molecular mechanisms underlying calcium mobilization. In SMCs,  $IP_3$  variations reflect the activation of G-protein-coupled receptors and subsequent release of calcium from intracellular stores, such as the sarcoplasmic reticulum. In ECs,  $IP_3$  signaling serves as a critical intermediary, linking upstream signaling events to calcium mobilization and facilitating the generation of calcium waves along the endothelium. These signaling dynamics underscore the intricate interplay between SMCs and ECs, which is essential for maintaining vascular homeostasis and adapting to local metabolic demands.

Figure 13 presents the dynamic changes in blood vessel radius as a result of neurovascular coupling. The variations in vessel radius reflect the synergistic effects of calcium and  $IP_3$  signaling on vascular tone regulation. Vasodilation and vasoconstriction are observed in response to these intracellular signals, demonstrating the capacity of the vascular network to adapt to changes in neuronal and glial activity. This response ensures efficient oxygen and nutrient delivery to tissues, particularly in metabolically active regions.

The results depicted in these figures validate the integrated neurovascular model by reproducing key physiological behaviors observed in experimental studies. The cou-

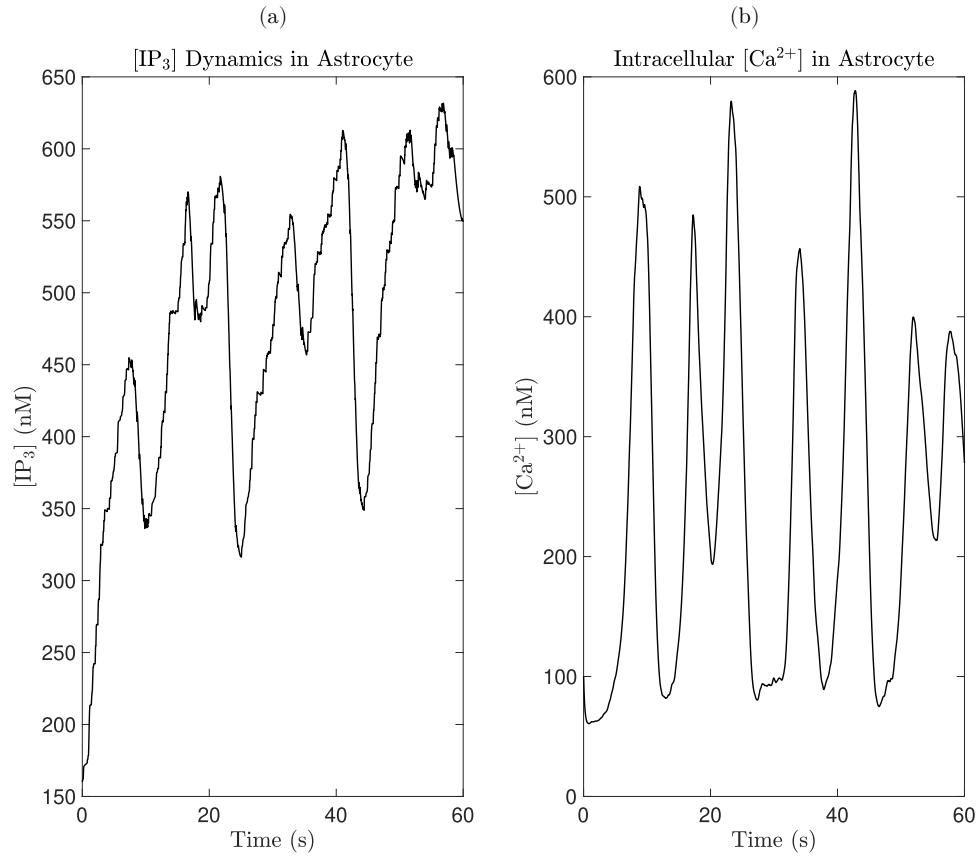


Fig. 11: Astrocytic signaling dynamics. (a)  $[IP_3]$  concentration in astrocytes as a response to neuronal activation. (b) Intracellular calcium concentration, showing the biphasic nature of calcium signaling in astrocytes.

pling between neuronal activation, astrocytic signaling, and vascular responses provides a comprehensive framework for understanding neurovascular coupling mechanisms and their implications in health and disease.

#### 4.6 Microcirculation on a Representative Unit of the DVC

Our computations extend the geometry of the *brain99* dataset to simulate the electromechanical coupling between neuro-glial activity and vascularization within the DVC. This model specifically captures the interaction between astrocytic and neuronal activity and the resulting dynamic changes in blood vessel radii. Blood flow dynamics and oxygen transport are analyzed within the vascular network to assess the influence of neuro-glial signals on vascular responses. The results demonstrate how capillary networks adapt

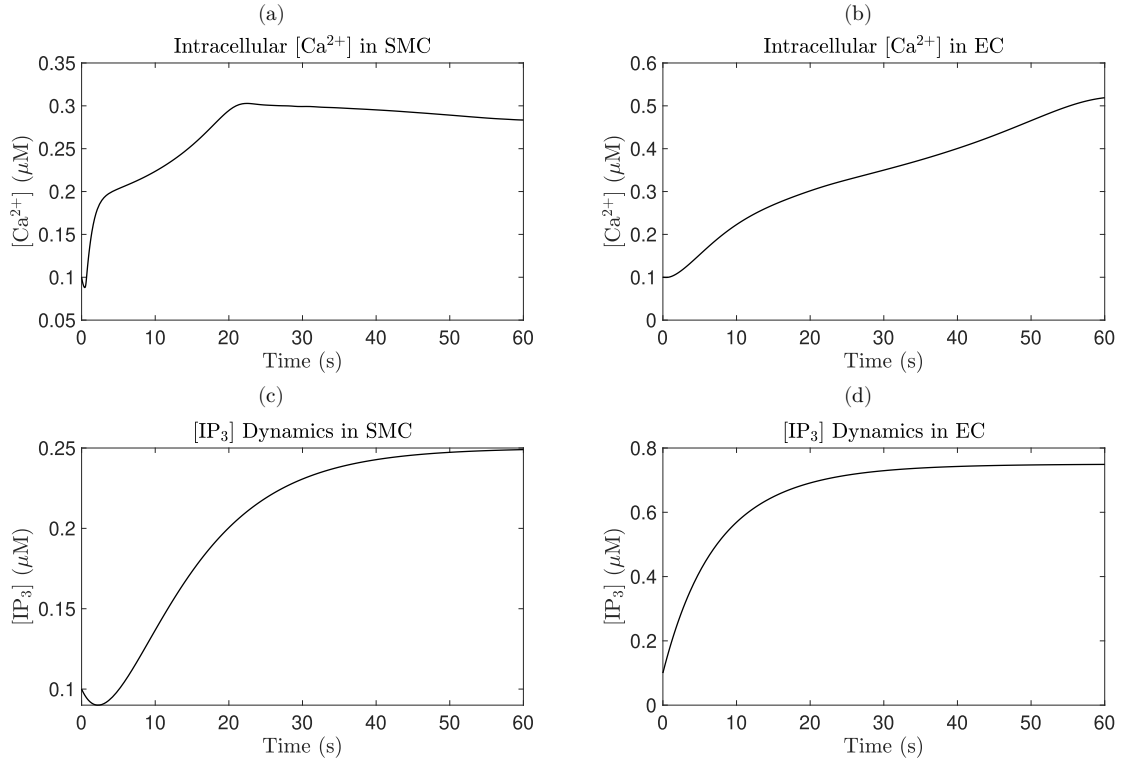


Fig. 12: Calcium and  $\text{IP}_3$  dynamics in vascular cells: (a) and (b), intracellular calcium concentration in SMCs and endothelial cells, alongside (c) and (d),  $\text{IP}_3$  signaling dynamics in these cells, highlighting the molecular interplay driving vascular responses.

to facilitate metabolic activity and neuronal function, while the hierarchical vascular structure ensures efficient blood supply and flow redistribution. This study particularly highlights the integration of macro- and microcirculation models to validate the mechanistic framework for neuro-glial-vascular coupling in the DVC.

The figures below illustrate the temporal evolution of blood flow patterns (Figure 14) and oxygen distribution (Figure 15) within the DVC microvascular network. These results reveal spatiotemporal variations in hemodynamics and oxygen delivery, computed based on the coupled neuro-glial-vascular framework. Figure 14 highlights how neuro-glial activity drives dynamic changes in blood flow, with vessel dilation and constriction contributing to flow redistribution across the network. Similarly, Figure 15 visualizes oxygen transport and diffusion within the vascular network and surrounding tissue, emphasizing the role of capillaries in ensuring adequate oxygenation. Together, these simulations provide detailed insights into the dynamic interplay between neuronal activation, astrocytic metabolism, and vascular responses within the DVC.

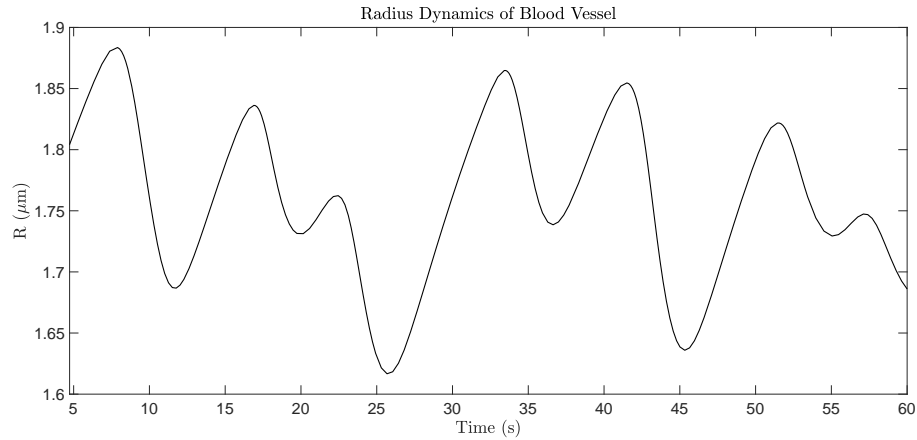


Fig. 13: Temporal changes in blood vessel radius under neurovascular coupling dynamics. The vessel radius is allowed to settle during the first 5 seconds before dynamic fluctuations occur. These changes illustrate the interaction between intracellular signaling and vascular tone regulation, exemplifying the capillary vessel where the arterial inflow is provided.

## 5 Discussion

The numerical results presented in this work illustrate how the integration of neuronal activity, astrocytic signaling, and vascular dynamics can yield a comprehensive understanding of neuro-glial-vascular interactions in the DVC. By simulating the interplay between excitatory and inhibitory neurotransmitters, neuron-astrocyte calcium signaling, and blood vessel tone regulation, our model captures key physiological features of functional hyperemia, highlighting the system's ability to meet local metabolic demands. The seamless coupling of synaptic events, astrocytic gliotransmitter release, and vascular responses underscores the intricate regulatory feedback loops that govern cerebral blood flow in health and disease.

Despite these promising findings, certain limitations must be acknowledged. The current study relies on simplified geometries and assumptions for macrocirculation, and we have primarily focused on the microcirculatory block derived from the *brain99* dataset. While this approach allows for computational tractability, future models should incorporate more detailed anatomical reconstructions and account for heterogeneities at

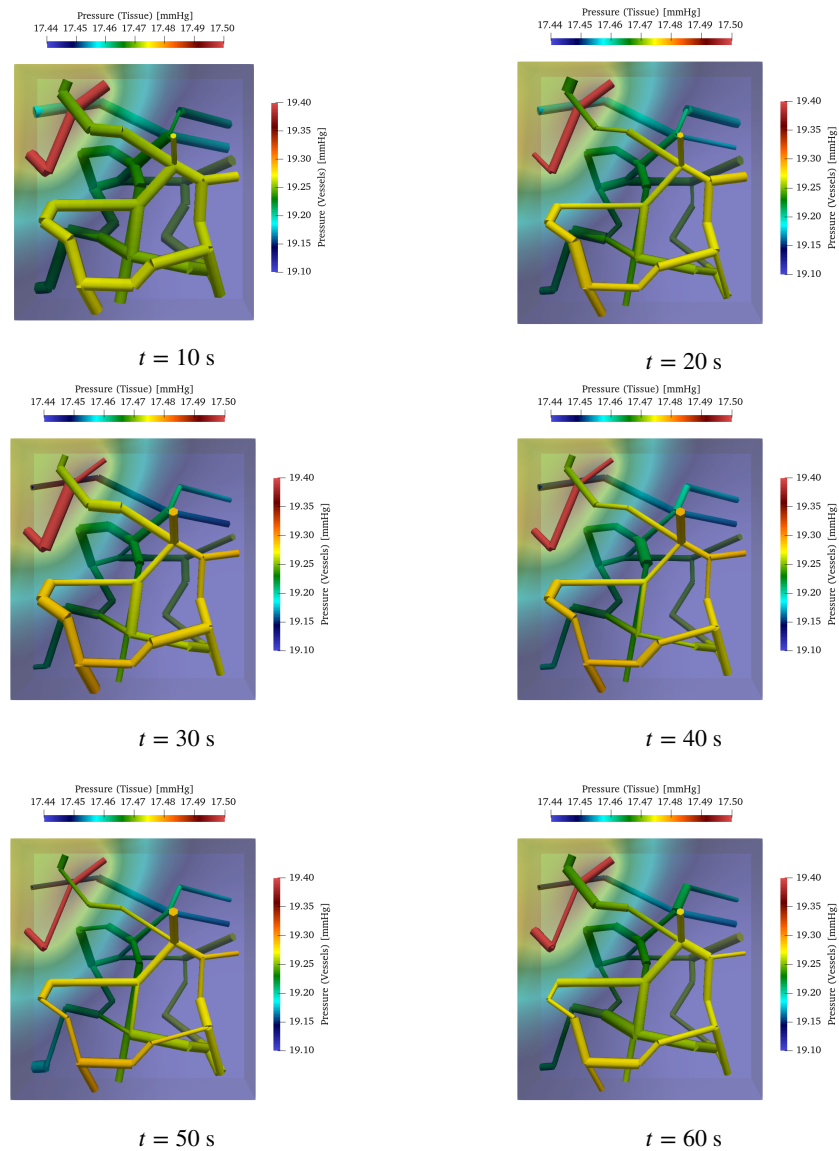


Fig. 14: Time-resolved simulation results of blood flow within the DVC microcirculation network. A cross-sectional view is obtained by slicing the computational unit (a unit cube) along its central horizontal plane. The color map represents the local blood flow velocity magnitude, highlighting how neuro–glial–vascular coupling causes dynamic redistribution of flow via vessel dilation and constriction in both capillaries and larger vessels.

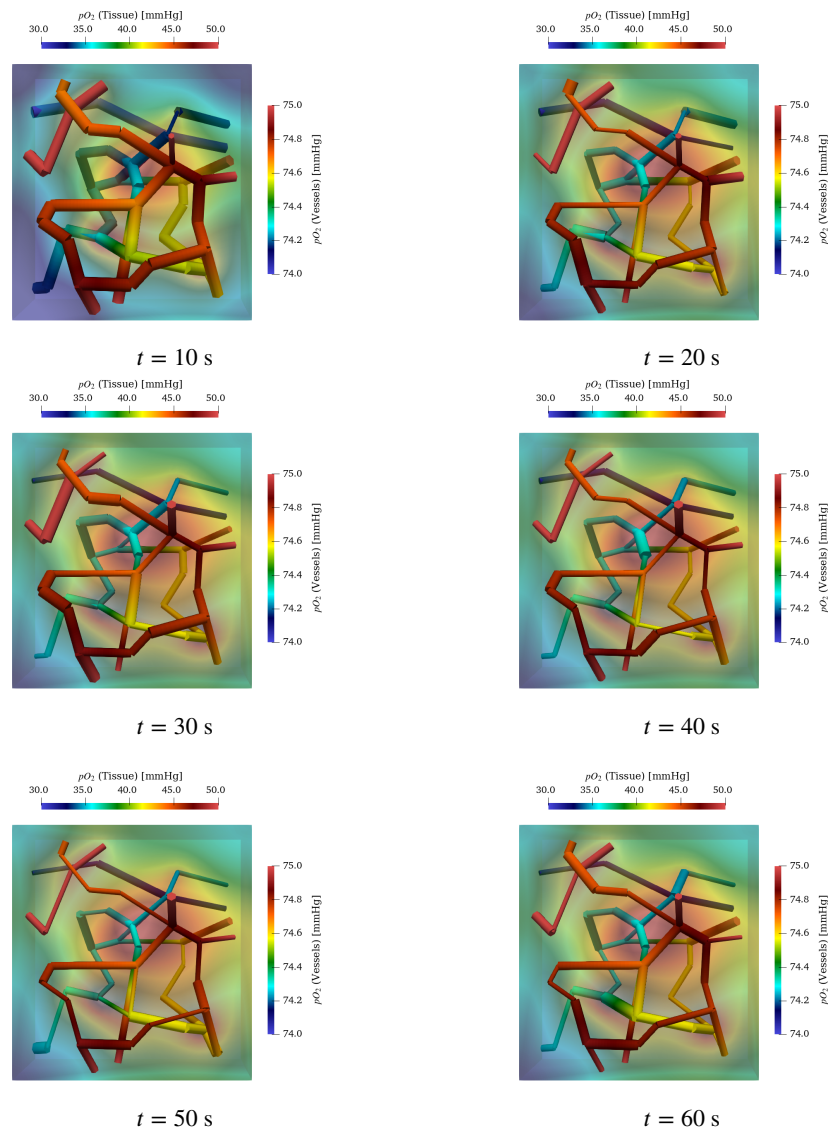


Fig. 15: Time-resolved simulation results of oxygen distribution within the DVC microcirculation network. A cross-sectional slice through the center of the computational domain (unit cube) is rendered in 3D, with colors indicating the oxygen partial pressure ( $pO_2$ ) in blood vessels and the surrounding tissue. This view captures the dynamics of oxygen delivery and diffusion via the 1D–3D coupling model, illustrating the impact of vessel diameter changes driven by neuro–glial interactions.

multiple scales (e.g., morphological variations in larger vessels or region-specific neuronal phenotypes). Additionally, improving the fidelity of cell-specific kinetics and including metabolic constraints—such as oxygen and glucose availability—could further enhance the model’s predictive power. These refinements would help bridge gaps between *in silico* analyses and *in vivo* observations, facilitating better translation to clinical and experimental contexts.

## 6 Conclusion

In conclusion, we have developed a modular, multi-scale modeling framework that unifies neuronal spiking, astrocytic calcium dynamics, and vascular tone regulation within the dorsal vagal complex. Our work introduces a coupled multi-scale model that provides a seamless transition from systemic hemodynamics to local capillary dynamics. In this framework, models for flow and transport of different dimensions are coupled, resulting in a 3D-1D-0D system. By embedding a quadripartite synapse model and linking it to a macro-/microcirculatory description, we demonstrate that neuro-glial-vascular coupling emerges through highly interactive feedback processes. The proposed approach provides a valuable and novel platform for studying functional hyperemia, investigating pathological disruptions of neurovascular homeostasis, and designing future experiments. Importantly, this work represents the first integrated model of its kind for the DVC, quantitatively capturing the interplay among neural, glial, and vascular components. Our simulation results reproduce physiologically realistic hemodynamic and synaptic behaviors in accordance with established textbook data, providing an initial validation of the model. We envisage that further refinement and extension of this model, for example by including patient-specific characteristics such as receptor heterogeneity, will offer deeper insights into cerebrovascular regulation and guide novel therapeutic strategies for various neurological conditions. Moreover, our simulation results establish a robust computational foundation for future translational investigations into both normal and pathological brain function. Finally, the generality of our methodology indicates that a similar modeling framework can be applied to other cortical areas, further broadening the scope of neurovascular research.

## Acknowledgments

This work was supported by the Deutsche Forschungsgemeinschaft (DFG, German Research Foundation) under project numbers 470246804 and 469698389, and through the International Graduate School of Science and Engineering (IGSSE) under project numbers WO 671/11-1 and WO 671/20-1. This research was supported by the IDIR-Project (Digital Implant Research), a cooperation financed by Kiel University, University Hospital Schleswig-Holstein and Helmholtz Zentrum Hereon.

## Declarations

The authors declare that they have no conflict of interest to disclose.

## Bibliography

- [1] JPKH Alastruey, KH Parker, J Peiró, SM Byrd, and SJ Sherwin. Modelling the circle of willis to assess the effects of anatomical variations and occlusions on cerebral flows. *Journal of biomechanics*, 40(8):1794–1805, 2007.
- [2] Wendy K Alderton, Chris E Cooper, and Richard G Knowles. Nitric oxide synthases: structure, function and inhibition. *Biochemical journal*, 357(3):593–615, 2001.
- [3] Joji Ando and Kimiko Yamamoto. Flow detection and calcium signalling in vascular endothelial cells. *Cardiovascular research*, 99(2):260–268, 2013.
- [4] Oluwatobi Ariyo and Farhana Akter. Anatomy and physiology of the neuron. *Neuroscience for Neurosurgeons*, page 72, 2024.
- [5] Katherine T Baldwin, Keith K Murai, and Baljit S Khakh. Astrocyte morphology. *Trends in Cell Biology*, 34(7):547–565, 2024.
- [6] Jill N Barnes and Nisha Charkoudian. Integrative cardiovascular control in women: regulation of blood pressure, body temperature and cerebrovascular responsiveness. *FASEB journal: official publication of the Federation of American Societies for Experimental Biology*, 35(2):e21143, 2021.
- [7] H. Bayir. Reactive oxygen species. *Crit Care Med*, 33(12 Suppl):S498–S501, Dec 2005.
- [8] Omer Ali Bayraktar, Theresa Bartels, Staffan Holmqvist, Vitalii Kleshchevnikov, Araks Martirosyan, Damon Polioudakis, Lucile Ben Haim, Adam MH Young, Mykhailo Y Batiuk, Kirti Prakash, et al. Astrocyte layers in the mammalian cerebral cortex revealed by a single-cell in situ transcriptomic map. *Nature neuroscience*, 23(4):500–509, 2020.
- [9] David J Begley and Milton W Brightman. Structural and functional aspects of the blood-brain barrier. *Peptide transport and delivery into the central nervous system*, pages 39–78, 2003.
- [10] Eduardo E Benarroch. *Basic neurosciences with clinical applications*. Elsevier Health Sciences, 2006.
- [11] Angelito A Bernardo, Christian M Bernardo, Doris Joy Espiritu, and Jose AL Ar-ruda. The sodium bicarbonate cotransporter: structure, function, and regulation. In *Seminars in nephrology*, volume 26, pages 352–360. Elsevier, 2006.
- [12] Richard Bertram, Arthur Sherman, and ELIS F Stanley. Single-domain/bound calcium hypothesis of transmitter release and facilitation. *Journal of Neurophysiology*, 75(5):1919–1931, 1996.
- [13] Paola Bezzi, Vidar Gundersen, José Luis Galbete, Gerald Seifert, Christian Steinhäuser, Ethel Pilati, and Andrea Volterra. Astrocytes contain a vesicular compartment that is competent for regulated exocytosis of glutamate. *Nature neuroscience*, 7(6):613–620, 2004.
- [14] Paola Bezzi and Andrea Volterra. A neuron–glia signalling network in the active brain. *Current opinion in neurobiology*, 11(3):387–394, 2001.
- [15] Kyle R Biesecker, Anja I Srienc, Angela M Shimoda, Amit Agarwal, Dwight E Bergles, Paulo Kofuji, and Eric A Newman. Glial cell calcium signaling medi-

- ates capillary regulation of blood flow in the retina. *Journal of Neuroscience*, 36(36):9435–9445, 2016.
- [16] Kim T Blackwell. Modeling calcium concentration and biochemical reactions. *Brains, Minds, and Media [Internet]*, 1:1–27, 2005.
- [17] Johann H Bollmann, Bert Sakmann, and J Gerard G Borst. Calcium sensitivity of glutamate release in a calyx-type terminal. *Science*, 289(5481):953–957, 2000.
- [18] Martin D Bootman, Michael J Berridge, and H Llewelyn Roderick. Calcium signalling: more messengers, more channels, more complexity. *Current Biology*, 12(16):R563–R565, 2002.
- [19] Ralf Brandes, Florian Lang, and Robert F Schmidt. *Physiologie des Menschen: mit Pathophysiologie*. Springer-Verlag, 2019.
- [20] Alexey Brazhe, Andrey Verisokin, Darya Vervevko, and Dmitry Postnov. Astrocytes: new evidence, new models, new roles. *Biophysical Reviews*, 15(5):1303–1333, 2023.
- [21] Eric A Bushong, Maryann E Martone, Ying Z Jones, and Mark H Ellisman. Protoplasmic astrocytes in cal stratum radiatum occupy separate anatomical domains. *Journal of Neuroscience*, 22(1):183–192, 2002.
- [22] Changsi Cai, Jonas C Fordsmann, Sofie H Jensen, Bodil Gesslein, Micael Lønstrup, Bjørn O Hald, Stefan A Zambach, Birger Brodin, and Martin J Lauritzen. Stimulation-induced increases in cerebral blood flow and local capillary vasoconstriction depend on conducted vascular responses. *Proceedings of the National Academy of Sciences*, 115(25):E5796–E5804, 2018.
- [23] S. Čanić and E. Kim. Mathematical analysis of the quasilinear effects in a hyperbolic model blood flow through compliant axi-symmetric vessels. *Mathematical Methods in the Applied Sciences*, 26(14):1161–1186, 2003.
- [24] Hua Chai, Blanca Diaz-Castro, Eiji Shigetomi, Emma Monte, J Christopher O'ceau, Xinzhu Yu, Whitaker Cohn, Pradeep S Rajendran, Thomas M Vondriska, Julian P Whitelegge, et al. Neural circuit-specialized astrocytes: transcriptomic, proteomic, morphological, and functional evidence. *Neuron*, 95(3):531–549, 2017.
- [25] Navdeep S Chandel. Glycolysis. *Cold Spring Harbor Perspectives in Biology*, 13(5):a040535, 2021.
- [26] Jingbo Chen, Yan Zhou, Shuying Liu, and Chaohong Li. Biomechanical signal communication in vascular smooth muscle cells. *Journal of Cell Communication and Signaling*, 14(4):357–376, 2020.
- [27] Kejing Chen and Aleksander S Popel. Theoretical analysis of biochemical pathways of nitric oxide release from vascular endothelial cells. *Free Radical Biology and Medicine*, 41(4):668–680, 2006.
- [28] Xi Chen, Tamás I Józsa, Danilo Cardim, Chiara Robba, Marek Czosnyka, and Stephen J Payne. Modelling midline shift and ventricle collapse in cerebral oedema following acute ischaemic stroke. *PLOS Computational Biology*, 20(5):e1012145, 2024.
- [29] Hannah Choi and Stefan Mihalas. Synchronization dependent on spatial structures of a mesoscopic whole-brain network. *PLoS computational biology*, 15(4):e1006978, 2019.
- [30] Eric H Chudler. Brain facts and figures. *Cerebral Cortex*, 31:77, 2013.

- [31] Jurgen AHR Claassen, Dick HJ Thijssen, Ronney B Panerai, and Frank M Faraci. Regulation of cerebral blood flow in humans: physiology and clinical implications of autoregulation. *Physiological reviews*, 101(4):1487–1559, 2021.
- [32] JD Clements. Transmitter timecourse in the synaptic cleft: its role in central synaptic function. *Trends in neurosciences*, 19(5):163–171, 1996.
- [33] William T Coffey, Yu P Kalmykov, and John T Waldron. *The Langevin equation: with applications to stochastic problems in physics, chemistry and electrical engineering*. World Scientific, 2004.
- [34] Jay S Coggan, Daniel Keller, Corrado Calì, Heikki Lehväslaiho, Henry Markram, Felix Schürmann, and Pierre J Magistretti. Norepinephrine stimulates glycogenolysis in astrocytes to fuel neurons with lactate. *PLoS computational biology*, 14(8):e1006392, 2018.
- [35] A. Comerford, M. J. Plank, and T. David. Endothelial nitric oxide synthase and calcium production in arterial geometries: An integrated fluid mechanics/cell model. *Journal of Biomechanical Engineering*, 130(1):011010, 2008.
- [36] Sonia Cortassa, Miguel A Aon, and Steven J Sollott. Control and regulation of substrate selection in cytoplasmic and mitochondrial catabolic networks. a systems biology analysis. *Frontiers in Physiology*, 10:201, 2019.
- [37] Niels C Danbolt. Glutamate uptake. *Progress in neurobiology*, 65(1):1–105, 2001.
- [38] Carlo D’Angelo. *Multiscale Modelling of Metabolism and Transport Phenomena in Living Tissues*. PhD thesis, École Polytechnique Fédérale de Lausanne, 2007.
- [39] Michael J Davis and Robert W Gore. Capillary pressures in rat intestinal muscle and mucosal villi during venous pressure elevation. *American Journal of Physiology-Heart and Circulatory Physiology*, 249(1):H174–H187, 1985.
- [40] Maurizio De Pittà, Mati Goldberg, Vladislav Volman, Hugues Berry, and Eshel Ben-Jacob. Glutamate regulation of calcium and ip 3 oscillating and pulsating dynamics in astrocytes. *Journal of biological physics*, 35:383–411, 2009.
- [41] Maurizio De Pittà, Vladislav Volman, Hugues Berry, and Eshel Ben-Jacob. A tale of two stories: astrocyte regulation of synaptic depression and facilitation. *PLoS computational biology*, 7(12):e1002293, 2011.
- [42] Alain Destexhe, Zachary F Mainen, Terrence J Sejnowski, et al. Kinetic models of synaptic transmission. *Methods in neuronal modeling*, 2:1–25, 1998.
- [43] Lynn E Dobrunz, Emily P Huang, and Charles F Stevens. Very short-term plasticity in hippocampal synapses. *Proceedings of the national academy of sciences*, 94(26):14843–14847, 1997.
- [44] K Dormanns, RG Brown, and T David. The role of nitric oxide in neurovascular coupling. *Journal of theoretical biology*, 394:1–17, 2016.
- [45] K Dormanns, EMJ van Disseldorp, RG Brown, and T David. Neurovascular coupling and the influence of luminal agonists via the endothelium. *Journal of theoretical biology*, 364:49–70, 2015.
- [46] Sonia Duchemin, Michaël Boily, Nataliya Sadekova, and Hélène Girouard. The complex contribution of nos interneurons in the physiology of cerebrovascular regulation. *Frontiers in neural circuits*, 6:51, 2012.
- [47] Wahbi K El-Bouri, Andrew MacGowan, Tamás I Józsa, Matthew J Gounis, and Stephen J Payne. Modelling the impact of clot fragmentation on the microcirculation after thrombectomy. *PLOS Computational Biology*, 17(3):e1008515, 2021.

- [48] Jan Willem Elting, Marit L Sanders, Ronney B Panerai, Marcel Aries, Edson Bor-Seng-Shu, Alexander Caicedo, Max Chacon, Erik D Gommer, Sabine Van Huffel, José L Jara, et al. Assessment of dynamic cerebral autoregulation in humans: Is reproducibility dependent on blood pressure variability? *PLoS One*, 15(1):e0227651, 2020.
- [49] Geoffrey G Emerson and Steven S Segal. Electrical coupling between endothelial cells and smooth muscle cells in hamster feed arteries: role in vasomotor control. *Circulation research*, 87(6):474–479, 2000.
- [50] Geoffrey G Emerson and Steven S Segal. Endothelial cell pathway for conduction of hyperpolarization and vasodilation along hamster feed artery. *Circulation research*, 86(1):94–100, 2000.
- [51] Nigel J Emptage, Christopher A Reid, and Alan Fine. Calcium stores in hippocampal synaptic boutons mediate short-term plasticity, store-operated  $ca^{2+}$  entry, and spontaneous transmitter release. *Neuron*, 29(1):197–208, 2001.
- [52] Jason G Emsley and Jeffrey D Macklis. Astroglial heterogeneity closely reflects the neuronal-defined anatomy of the adult murine CNS. *Neuron glia biology*, 2(3):175–186, 2006.
- [53] Frido Erler, Michael Meyer-Hermann, and Gerhard Soff. A quantitative model for presynaptic free  $ca^{2+}$  dynamics during different stimulation protocols. *Neurocomputing*, 61:169–191, 2004.
- [54] Christopher P Fall, Eric S Marland, John M Wagner, and John J Tyson. Computational cell biology. *New York*, 2002.
- [55] Tommaso Fellin. Communication between neurons and astrocytes: relevance to the modulation of synaptic and network activity. *Journal of neurochemistry*, 108(3):533–544, 2009.
- [56] Alisdair R Fernie, Fernando Carrari, and Lee J Sweetlove. Respiratory metabolism: glycolysis, the tca cycle and mitochondrial electron transport. *Current opinion in plant biology*, 7(3):254–261, 2004.
- [57] Alisdair R Fernie and Enrico Martinoia. Malate. jack of all trades or master of a few? *Phytochemistry*, 70(7):828–832, 2009.
- [58] Jessica A Filosa, Adrian D Bonev, Stephen V Straub, Andrea L Meredith, M Keith Wilkerson, Richard W Aldrich, and Mark T Nelson. Local potassium signaling couples neuronal activity to vasodilation in the brain. *Nature neuroscience*, 9(11):1397–1403, 2006.
- [59] Jessica A Filosa, Helena W Morrison, Jennifer A Iddings, Wenting Du, and Ki Jung Kim. Beyond neurovascular coupling, role of astrocytes in the regulation of vascular tone. *Neuroscience*, 323:96–109, 2016.
- [60] Ingrid Fleming and Rudi Busse. No: the primary edrf. *Journal of molecular and cellular cardiology*, 31(1):5–14, 1999.
- [61] Ulrich Förstermann, Jean-Paul Boissel, and Hartmut Kleinert. Expressional control of the ‘constitutive’ isoforms of nitric oxide synthase (nos i and nos iii). *The FASEB Journal*, 12(10):773–790, 1998.
- [62] Paul Forsythe, Mark Gilchrist, Marianne Kulka, and A Dean Befus. Mast cells and nitric oxide: control of production, mechanisms of response. *International immunopharmacology*, 1(8):1525–1541, 2001.

- [63] Kevin M Franks, Thomas M Bartol, and Terrence J Sejnowski. A monte carlo model reveals independent signaling at central glutamatergic synapses. *Biophysical journal*, 83(5):2333–2348, 2002.
- [64] Marvin Fritz, Tobias Köppl, John Tinsley Oden, Andreas Wagner, Barbara Wohlmuth, and Chengyue Wu. A 1d–0d–3d coupled model for simulating blood flow and transport processes in breast tissue. *International Journal for Numerical Methods in Biomedical Engineering*, 38(7):e3612, 2022.
- [65] Robert F Furchgott and John V Zawadzki. The obligatory role of endothelial cells in the relaxation of arterial smooth muscle by acetylcholine. *nature*, 288(5789):373–376, 1980.
- [66] Robert H Garman. Histology of the central nervous system. *Toxicologic pathology*, 39(1):22–35, 2011.
- [67] Ja Garthwaite and CL Boulton. Nitric oxide signaling in the central nervous system. *Annual review of physiology*, 57(1):683–706, 1995.
- [68] Srinivas Ghatta, Deepthi Nimmagadda, Xiaoping Xu, and Stephen T O’Rourke. Large-conductance, calcium-activated potassium channels: structural and functional implications. *Pharmacology & therapeutics*, 110(1):103–116, 2006.
- [69] Stefano Ghisla. Beta-oxidation of fatty acids. a century of discovery. *European Journal of Biochemistry*, 271(3):459–461, 2004.
- [70] Julianna Goenaga, Alfonso Araque, Paulo Kofuji, and Daniela Herrera Moro Chao. Calcium signaling in astrocytes and gliotransmitter release. *Frontiers in synaptic neuroscience*, 15:1138577, 2023.
- [71] Albert Goldbeter, Geneviève Dupont, and Michael J Berridge. Minimal model for signal-induced  $ca^{2+}$  oscillations and for their frequency encoding through protein phosphorylation. *Proceedings of the National Academy of Sciences*, 87(4):1461–1465, 1990.
- [72] Chi-Ming Hai and Richard A Murphy. Cross-bridge phosphorylation and regulation of latch state in smooth muscle. *American Journal of Physiology-Cell Physiology*, 254(1):C99–C106, 1988.
- [73] Chi-ming Hai and Richard A Murphy.  $Ca^{2+}$  crossbridge phosphorylation, and contraction. *Annual review of physiology*, 51(1):285–298, 1989.
- [74] Catherine N Hall, Clare Reynell, Bodil Gesslein, Nicola B Hamilton, Anusha Mishra, Brad A Sutherland, Fergus M O’Farrell, Alastair M Buchan, Martin Lauritzen, and David Attwell. Capillary pericytes regulate cerebral blood flow in health and disease. *Nature*, 508(7494):55–60, 2014.
- [75] K Harris and SB Kater. Dendritic spines: cellular specializations imparting both stability and flexibility to synaptic function. *Annual review of neuroscience*, 17(1):341–371, 1994.
- [76] David A Hartmann, Robert G Underly, Roger I Grant, Ashley N Watson, Volkhard Lindner, and Andy Y Shih. Pericyte structure and distribution in the cerebral cortex revealed by high-resolution imaging of transgenic mice. *Neurophotonics*, 2(4):041402–041402, 2015.
- [77] Aurélie Hautefort, Anna Pfenniger, and Brenda R Kwak. Endothelial connexins in vascular function. *Vascular Biology*, 1(1):H117–H124, 2019.
- [78] Peter C Heinrich, Matthias Müller, and Lutz Graeve. *Löffler/Petrides Biochemie und Pathobiochemie*. Springer-Verlag, 2014.

- [79] Hiroshi Hibino, Atsushi Inanobe, Kazuharu Furutani, Shingo Murakami, IAN Findlay, and Yoshihisa Kurachi. Inwardly rectifying potassium channels: their structure, function, and physiological roles. *Physiological reviews*, 90(1):291–366, 2010.
- [80] David C Hill-Eubanks, Albert L Gonzales, Swapnil K Sonkusare, and Mark T Nelson. Vascular trp channels: performing under pressure and going with the flow. *Physiology*, 29(5):343–360, 2014.
- [81] Alan L Hodgkin and Andrew F Huxley. A quantitative description of membrane current and its application to conduction and excitation in nerve. *The Journal of physiology*, 117(4):500, 1952.
- [82] Lynne A Holtzclaw, Siddhesh Pandhit, Dan J Bare, Gregory A Mignery, and James T Russell. Astrocytes in adult rat brain express type 2 inositol 1, 4, 5-trisphosphate receptors. *Glia*, 39(1):69–84, 2002.
- [83] T. Hughes and J. Lubliner. On the one-dimensional theory of blood flow in the larger vessels. *Mathematical Biosciences*, 18(1):161–170, 1973.
- [84] Costantino Iadecola. Regulation of the cerebral microcirculation during neural activity: is nitric oxide the missing link? *Trends in neurosciences*, 16(6):206–214, 1993.
- [85] Costantino Iadecola. The neurovascular unit coming of age: a journey through neurovascular coupling in health and disease. *Neuron*, 96(1):17–42, 2017.
- [86] Satoshi Ii, Hiroki Kitade, Shunichi Ishida, Yohsuke Imai, Yoshiyuki Watanabe, and Shigeo Wada. Multiscale modeling of human cerebrovasculature: A hybrid approach using image-based geometry and a mathematical algorithm. *PLoS computational biology*, 16(6):e1007943, 2020.
- [87] Taro Ishikawa, Masahiro Kaneko, Hee-Sup Shin, and Tomoyuki Takahashi. Presynaptic n-type and p/q-type  $ca^{2+}$  channels mediating synaptic transmission at the calyx of held of mice. *The Journal of physiology*, 568(1):199–209, 2005.
- [88] Masaaki Ito and David J Hartshorne. Phosphorylation of myosin as a regulatory mechanism in smooth muscle. *Progress in clinical and biological research*, 327:57–72, 1990.
- [89] Craig E Jahr and Charles F Stevens. Calcium permeability of the n-methyl-d-aspartate receptor channel in hippocampal neurons in culture. *Proceedings of the National Academy of Sciences*, 90(24):11573–11577, 1993.
- [90] Thomas P Jensen, Adelaida G Filoteo, Thomas Knopfel, and Ruth M Emsen. Presynaptic plasma membrane  $ca^{2+}$  atpase isoform 2a regulates excitatory synaptic transmission in rat hippocampal  $ca3$ . *The Journal of physiology*, 579(1):85–99, 2007.
- [91] Robinson Joannides, Walter E Haefeli, Lilly Linder, Vincent Richard, El Hassan Bakkali, Christian Thuillez, and Thomas F Lüscher. Nitric oxide is responsible for flow-dependent dilatation of human peripheral conduit arteries in vivo. *Circulation*, 91(5):1314–1319, 1995.
- [92] Kamel Kacem, Pierre Lacombe, Jacques Seylaz, and Gilles Bonvento. Structural organization of the perivascular astrocyte endfeet and their relationship with the endothelial glucose transporter: a confocal microscopy study. *Glia*, 23(1):1–10, 1998.

- [93] Jian Kang, Li Jiang, Steven A Goldman, and Maiken Nedergaard. Astrocyte-mediated potentiation of inhibitory synaptic transmission. *Nature neuroscience*, 1(8):683–692, 1998.
- [94] Jian Kang, Ning Kang, Ditte Lovatt, Arnulfo Torres, Zhuo Zhao, Jane Lin, and Maiken Nedergaard. Connexin 43 hemichannels are permeable to atp. *Journal of Neuroscience*, 28(18):4702–4711, 2008.
- [95] Mahendra Kavdia, Nikolaos M Tsoukias, and Aleksander S Popel. Model of nitric oxide diffusion in an arteriole: impact of hemoglobin-based blood substitutes. *American Journal of Physiology-Heart and Circulatory Physiology*, 282(6):H2245–H2253, 2002.
- [96] James Keener and James Sneyd. *Mathematical physiology: II: Systems physiology*. Springer, 2009.
- [97] Hyunsook Kim, Byung-Hwan Lee, Sun-Hye Choi, Hyeon-Joong Kim, Suk-Won Jung, Sung-Hee Hwang, Hyewon Rhim, Hyung-Chun Kim, Ik-Hyun Cho, and Seung-Yeol Nah. Gintonin stimulates gliotransmitter release in cortical primary astrocytes. *Neuroscience letters*, 603:19–24, 2015.
- [98] Sun Kwang Kim, Hideaki Hayashi, Tatsuya Ishikawa, Keisuke Shibata, Eiji Shigetomi, Youichi Shinozaki, Hiroyuki Inada, Seung Eon Roh, Sang Jeong Kim, Gihyun Lee, et al. Cortical astrocytes rewire somatosensory cortical circuits for peripheral neuropathic pain. *The Journal of clinical investigation*, 126(5):1983–1997, 2016.
- [99] Michèle Koenigsberger, Roger Sauser, Jean-Louis Bény, and Jean-Jacques Meister. Role of the endothelium on arterial vasomotion. *Biophysical journal*, 88(6):3845–3854, 2005.
- [100] Michèle Koenigsberger, Roger Sauser, Jean-Louis Bény, and Jean-Jacques Meister. Effects of arterial wall stress on vasomotion. *Biophysical journal*, 91(5):1663–1674, 2006.
- [101] Paulo Kofuji and EA2322935 Newman. Potassium buffering in the central nervous system. *Neuroscience*, 129(4):1043–1054, 2004.
- [102] Tobias Köppl and Rainer Helmig. *Dimension Reduced Modeling of Blood Flow in Large Arteries: An Introduction for Master Students and First Year Doctoral Students*. Springer Nature, 2023.
- [103] Tobias Köppl, Ettore Vidotto, and Barbara Wohlmuth. A 3d-1d coupled blood flow and oxygen transport model to generate microvascular networks. *International journal for numerical methods in biomedical engineering*, 36(10):e3386, 2020.
- [104] Yoshiyuki Kubota, Ryuichi Hattori, and Yoshiki Yui. Three distinct subpopulations of gabaergic neurons in rat frontal agranular cortex. *Brain research*, 649(1-2):159–173, 1994.
- [105] Jack R Lancaster Jr. Simulation of the diffusion and reaction of endogenously produced nitric oxide. *Proceedings of the National Academy of Sciences*, 91(17):8137–8141, 1994.
- [106] Hong-Hsi Lee, Katarina Yaros, Jelle Veraart, Jasmine L Pathan, Feng-Xia Liang, Sunghoon G Kim, Dmitry S Novikov, and Els Fieremans. Along-axon diameter variation and axonal orientation dispersion revealed with 3d electron microscopy: implications for quantifying brain white matter microstructure with histology and diffusion mri. *Brain Structure and Function*, 224:1469–1488, 2019.

- [107] Jaekwang Lee, Ye-Eun Chun, Kyung-Seok Han, Jungmoo Lee, Dong Ho Woo, and C Justin Lee. Ca<sup>2+</sup> entry is required for mechanical stimulation-induced atp release from astrocyte. *Experimental neurobiology*, 24(1):17, 2015.
- [108] Yue-Xian Li and John Rinzel. Equations for insp3 receptor-mediated [ca<sup>2+</sup>] i oscillations derived from a detailed kinetic model: a hodgkin-huxley like formalism. *Journal of theoretical Biology*, 166(4):461–473, 1994.
- [109] Thomas A Longden, Fabrice Dabertrand, Masayo Koide, Albert L Gonzales, Nathan R Tykocki, Joseph E Brayden, David Hill-Eubanks, and Mark T Nelson. Capillary k<sup>+</sup>-sensing initiates retrograde hyperpolarization to increase local cerebral blood flow. *Nature neuroscience*, 20(5):717–726, 2017.
- [110] Thomas A Longden and Mark T Nelson. Vascular inward rectifier k<sup>+</sup> channels as external k<sup>+</sup> sensors in the control of cerebral blood flow. *Microcirculation*, 22(3):183–196, 2015.
- [111] M Losada, M Hervas, MA De la Rosa, and FF De la Rosa. Energy transduction by bioelectrochemical systems. *Journal of electroanalytical chemistry and interfacial electrochemistry*, 156:193–230, 1983.
- [112] Shino D Magaki, Christopher K Williams, and Harry V Vinters. Glial function (and dysfunction) in the normal & ischemic brain. *Neuropharmacology*, 134:218–225, 2018.
- [113] Adam Mahdi, Jacob Sturdy, Johnny T Ottesen, and Mette S Olufsen. Modeling the afferent dynamics of the baroreflex control system. *PLoS computational biology*, 9(12):e1003384, 2013.
- [114] Erik B Malarkey and Vladimir Parpura. Temporal characteristics of vesicular fusion in astrocytes: examination of synaptobrevin 2-laden vesicles at single vesicle resolution. *The Journal of physiology*, 589(17):4271–4300, 2011.
- [115] T Malinski, F Bailey, ZG Zhang, and M Chopp. Nitric oxide measured by a porphyrinic micro sensor in rat brain after transient middle cerebral artery occlusion. *Journal of Cerebral Blood Flow & Metabolism*, 13(3):355–358, 1993.
- [116] Miguel Marín-Padilla. The human brain intracerebral microvascular system: development and structure. *Frontiers in neuroanatomy*, 6:38, 2012.
- [117] Thomas Misje Mathiisen, Knut Petter Lehre, Niels Christian Danbolt, and Ole Petter Ottersen. The perivascular astroglial sheath provides a complete covering of the brain microvessels: an electron microscopic 3d reconstruction. *Glia*, 58(9):1094–1103, 2010.
- [118] Bernd Mayer and Benjamin Hemmens. Biosynthesis and action of nitric oxide in mammalian cells. *Trends in biochemical sciences*, 22(12):477–481, 1997.
- [119] Anusha Mishra. Binaural blood flow control by astrocytes: listening to synapses and the vasculature. *The Journal of physiology*, 595(6):1885–1902, 2017.
- [120] Vedrana Montana, Erik B Malarkey, Claudia Verderio, Michela Matteoli, and Vladimir Parpura. Vesicular transmitter release from astrocytes. *Glia*, 54(7):700–715, 2006.
- [121] Christopher I Moore and Rosa Cao. The hemo-neural hypothesis: on the role of blood flow in information processing. *Journal of neurophysiology*, 99(5):2035–2047, 2008.
- [122] Enrico DF Motti, Hans-Georg Imhof, and M Gazi Yaşargil. The terminal vascular bed in the superficial cortex of the rat: an sem study of corrosion casts. *Journal of neurosurgery*, 65(6):834–846, 1986.

- [123] Cristin A Mount and Joe M Das. Cerebral perfusion pressure. In *StatPearls [Internet]*. StatPearls Publishing, 2023.
- [124] Cecil D Murray. The physiological principle of minimum work applied to the angle of branching of arteries. *The Journal of general physiology*, 9(6):835, 1926.
- [125] Cecil D Murray. The physiological principle of minimum work: I. the vascular system and the cost of blood volume. *Proceedings of the National Academy of Sciences*, 12(3):207–214, 1926.
- [126] Suhita Nadkarni and Peter Jung. Spontaneous oscillations of dressed neurons: a new mechanism for epilepsy? *Physical review letters*, 91(26):268101, 2003.
- [127] Suhita Nadkarni and Peter Jung. Modeling synaptic transmission of the tripartite synapse. *Physical biology*, 4(1):1, 2007.
- [128] Suhita Nadkarni, Peter Jung, and Herbert Levine. Astrocytes optimize the synaptic transmission of information. *PLoS computational biology*, 4(5):e1000088, 2008.
- [129] Eric A Newman. New roles for astrocytes: regulation of synaptic transmission. *Trends in neurosciences*, 26(10):536–542, 2003.
- [130] M. Olufsen. Structured tree outflow condition for blood flow in larger systemic arteries. *American Journal of Physiology-Heart and Circulatory Physiology*, 276(1):H257–H268, 1999.
- [131] Tomohiro Otani, Nozomi Nishimura, Hiroshi Yamashita, Satoshi Ii, Shigeki Yamada, Yoshiyuki Watanabe, Marie Oshima, and Shigeo Wada. Computational modeling of multiscale collateral blood supply in a whole-brain-scale arterial network. *PLOS Computational Biology*, 19(9):e1011452, 2023.
- [132] Surajit Panja, Sourav Patra, Anirban Mukherjee, Madhumita Basu, Sanghamitra Sengupta, and Pranab K Dutta. A closed-loop control scheme for steering steady states of glycolysis and glycogenolysis pathway. *IEEE/ACM Transactions on Computational Biology and Bioinformatics*, 10(4):858–868, 2013.
- [133] Achilles J. Pappano. 9 – the peripheral circulation and its control. In *Cardiovascular Physiology (Tenth Edition)*. Elsevier, 2013.
- [134] Vladimir Parpura, Trent A Basarsky, Fang Liu, Ksenija Jeftinija, Srdija Jeftinija, and Philip G Haydon. Glutamate-mediated astrocyte–neuron signalling. *Nature*, 369(6483):744–747, 1994.
- [135] Vladimir Parpura and Philip G Haydon. Physiological astrocytic calcium levels stimulate glutamate release to modulate adjacent neurons. *Proceedings of the National Academy of Sciences*, 97(15):8629–8634, 2000.
- [136] Dimitris Parthimos, David Hughes Edwards, and TM Griffith. Minimal model of arterial chaos generated by coupled intracellular and membrane  $Ca^{2+}$  oscillators. *American Journal of Physiology-Heart and Circulatory Physiology*, 277(3):H1119–H1144, 1999.
- [137] Claire M Peppiatt, Clare Howarth, Peter Mobbs, and David Attwell. Bidirectional control of cns capillary diameter by pericytes. *Nature*, 443(7112):700–704, 2006.
- [138] Gertrudis Perea and Alfonso Araque. Astrocytes potentiate transmitter release at single hippocampal synapses. *Science*, 317(5841):1083–1086, 2007.
- [139] Ognen AC Petroff. Book review: Gaba and glutamate in the human brain. *The Neuroscientist*, 8(6):562–573, 2002.

- [140] Aaron A Phillips, Franco HN Chan, Mei Mu Zi Zheng, Andrei V Krassioukov, and Philip N Ainslie. Neurovascular coupling in humans: physiology, methodological advances and clinical implications. *Journal of Cerebral Blood Flow & Metabolism*, 36(4):647–664, 2016.
- [141] James T Porter and Ken D McCarthy. Hippocampal astrocytes in situ respond to glutamate released from synaptic terminals. *Journal of Neuroscience*, 16(16):5073–5081, 1996.
- [142] Jessica L Presa, Flavia Saravia, Zsolt Bagi, and Jessica A Filosa. Vasculoneuronal coupling and neurovascular coupling at the neurovascular unit: impact of hypertension. *Frontiers in physiology*, 11:584135, 2020.
- [143] A. Pries, T. Secomb, and P. Gaehtgens. Biophysical aspects of blood flow in the microvasculature. *Cardiovascular Research*, 32(4):654–667, 1996.
- [144] Louis F Reichardt and Regis B Kelly. A molecular description of nerve terminal function. *Annual review of biochemistry*, 52:871, 1983.
- [145] Ravi L Rungta, Emmanuelle Chaigneau, Bruno-Félix Osmanski, and Serge Charpak. Vascular compartmentalization of functional hyperemia from the synapse to the pia. *Neuron*, 99(2):362–375, 2018.
- [146] John M Russell. Sodium-potassium-chloride cotransport. *Physiological reviews*, 80(1):211–276, 2000.
- [147] Daniela A Sahlender, Iaroslav Savtchouk, and Andrea Volterra. What do we know about gliotransmitter release from astrocytes? *Philosophical Transactions of the Royal Society B: Biological Sciences*, 369(1654):20130592, 2014.
- [148] M.A. Samuels, S.K. Feske, and K.R. Daffner. *Office Practice of Neurology*. MD Consult. Churchill Livingstone, 2003.
- [149] David M Santucci and Sridhar Raghavachari. The effects of nr2 subunit-dependent nmda receptor kinetics on synaptic transmission and camkii activation. *PLoS computational biology*, 4(10):e1000208, 2008.
- [150] Samantha Schaeffer and Costantino Iadecola. Revisiting the neurovascular unit. *Nature neuroscience*, 24(9):1198–1209, 2021.
- [151] TW Secomb, R Hsu, NB Beamer, and BM Coull. Theoretical simulation of oxygen transport to brain by networks of microvessels: effects of oxygen supply and demand on tissue hypoxia. *Microcirculation*, 7(4):237–247, 2000.
- [152] Alan E Senior, Sashi Nadanaciva, and Joachim Weber. The molecular mechanism of atp synthesis by f1f0-atp synthase. *Biochimica et Biophysica Acta (BBA)-Bioenergetics*, 1553(3):188–211, 2002.
- [153] Alexander Shapson-Coe, Michał Januszewski, Daniel R Berger, Art Pope, Yue-long Wu, Tim Blakely, Richard L Schalek, Peter H Li, Shuohong Wang, Jeremy Maitin-Shepard, et al. A petavoxel fragment of human cerebral cortex reconstructed at nanoscale resolution. *Science*, 384(6696):eadk4858, 2024.
- [154] Emanuele Sher, Erminio Biancardi, Maria Passafaro, and Francesco Clementi. Physiopathology of neuronal voltage-operated calcium channels. *The FASEB journal*, 5(12):2677–2683, 1991.
- [155] Mark W Sherwood, Misa Arizono, Aude Panatier, Katsuhiko Mikoshiba, and Stéphane HR Olié. Astrocytic ip3rs: Beyond ip3r2. *Frontiers in cellular neuroscience*, 15:695817, 2021.

- [156] Eiji Shigetomi, Sandip Patel, and Baljit S Khakh. Probing the complexities of astrocyte calcium signaling. *Trends in cell biology*, 26(4):300–312, 2016.
- [157] Jian-Wei Shuai and Peter Jung. Stochastic properties of  $ca^{2+}$  release of inositol 1, 4, 5-trisphosphate receptor clusters. *Biophysical journal*, 83(1):87–97, 2002.
- [158] Marie Simard, Gregory Arcuino, Takahiro Takano, Qing Song Liu, and Maiken Nedergaard. Signaling at the gliovascular interface. *Journal of Neuroscience*, 23(27):9254–9262, 2003.
- [159] J Sneyd and M Falcke. Models of the inositol trisphosphate receptor. *Progress in biophysics and molecular biology*, 89(3):207–245, 2005.
- [160] Seungkyu Son, Kenichiro Nagahama, Jinsu Lee, Kanghoon Jung, Chuljung Kwak, Jihoon Kim, Young Woo Noh, Eunjoon Kim, Sangkyu Lee, Hyung-Bae Kwon, et al. Real-time visualization of structural dynamics of synapses in live cells in vivo. *Nature Methods*, 21(2):353–360, 2024.
- [161] Anna Stincone, Alessandro Prigione, Thorsten Cramer, Mirjam MC Wamelink, Kate Campbell, Eric Cheung, Viridiana Olin-Sandoval, Nana-Maria Grüning, Antje Krüger, Mohammad Tauqeer Alam, et al. The return of metabolism: biochemistry and physiology of the pentose phosphate pathway. *Biological Reviews*, 90(3):927–963, 2015.
- [162] James D Stockand and Steven C Sansom. Mechanism of activation by cgmp-dependent protein kinase of large  $ca^{2+}$ -activated  $k^{+}$  channels in mesangial cells. *American Journal of Physiology-Cell Physiology*, 271(5):C1669–C1677, 1996.
- [163] Melanie D Sweeney, Zhen Zhao, Axel Montagne, Amy R Nelson, and Berislav V Zlokovic. Blood-brain barrier: from physiology to disease and back. *Physiological reviews*, 2018.
- [164] Shivendra G Tewari and Kaushik Kumar Majumdar. A mathematical model of the tripartite synapse: astrocyte-induced synaptic plasticity. *Journal of biological physics*, 38:465–496, 2012.
- [165] Pratish Thakore, Michael G Alvarado, Sher Ali, Amreen Mughal, Paulo W Pires, Evan Yamasaki, Harry AT Pritchard, Brant E Isakson, Cam Ha T Tran, and Scott Earley. Brain endothelial cell *trpa1* channels initiate neurovascular coupling. *elife*, 10:e63040, 2021.
- [166] Douglas D Thomas, Xiaoping Liu, Stephen P Kantrow, and Jack R Lancaster Jr. The biological lifetime of nitric oxide: implications for the perivascular dynamics of  $no$  and  $o_2$ . *Proceedings of the National Academy of Sciences*, 98(1):355–360, 2001.
- [167] Eleuterio F Toro. Brain venous haemodynamics, neurological diseases and mathematical modelling. A review. *Applied Mathematics and Computation*, 272:542–579, 2016.
- [168] Quang-Kim Tran, Kyoichi Ohashi, and Hiroshi Watanabe. Calcium signalling in endothelial cells. *Cardiovascular research*, 48(1):13–22, 2000.
- [169] Shreejoy J Tripathy, Lilah Toker, Brenna Li, Cindy-Lee Crichlow, Dmitry Tebaykin, B Ogan Mancarci, and Paul Pavlidis. Transcriptomic correlates of neuron electrophysiological diversity. *PLoS computational biology*, 13(10):e1005814, 2017.

- [170] Hui-Hsin Tsai, Huiliang Li, Luis C Fuentealba, Anna V Molofsky, Raquel Taveira-Marques, Helin Zhuang, April Tenney, Alice T Murnen, Stephen PJ Fancy, Florian Merkle, et al. Regional astrocyte allocation regulates cns synaptogenesis and repair. *Science*, 337(6092):358–362, 2012.
- [171] Misha V Tsodyks and Henry Markram. The neural code between neocortical pyramidal neurons depends on neurotransmitter release probability. *Proceedings of the national academy of sciences*, 94(2):719–723, 1997.
- [172] Vladislav Volman, Eshel Ben-Jacob, and Herbert Levine. The astrocyte as a gatekeeper of synaptic information transfer. *Neural computation*, 19(2):303–326, 2007.
- [173] TM Zaved Waise, Helen J Dranse, and Tony KT Lam. The metabolic role of vagal afferent innervation. *Nature Reviews Gastroenterology & Hepatology*, 15(10):625–636, 2018.
- [174] Lu-Yang Wang, Michael J Fedchyshyn, and Yi-Mei Yang. Action potential evoked transmitter release in central synapses: insights from the developing calyx of held. *Molecular brain*, 2:1–11, 2009.
- [175] Alexander M Weber, Fiona K Wong, Adele R Tufford, Lyanne C Schlichter, Victor Matveev, and Elise F Stanley. N-type  $ca^{2+}$  channels carry the largest current: implications for nanodomains and transmitter release. *Nature neuroscience*, 13(11):1348–1350, 2010.
- [176] Theodore F Wiesner, Bradford C Berk, and Robert M Nerem. A mathematical model of the cytosolic-free calcium response in endothelial cells to fluid shear stress. *Proceedings of the National Academy of Sciences*, 94(8):3726–3731, 1997.
- [177] Thomas N Wight. Arterial remodeling in vascular disease: a key role for hyaluronan and versican. *Frontiers in Bioscience-Landmark*, 13(13):4933–4937, 2008.
- [178] Ling-Gang Wu and J Gerard G Borst. The reduced release probability of releasable vesicles during recovery from short-term synaptic depression. *Neuron*, 23(4):821–832, 1999.
- [179] Yingfei Xiong, Sasa Teng, Lianghong Zheng, Suhua Sun, Jie Li, Ning Guo, Mingli Li, Li Wang, Feipeng Zhu, Changhe Wang, et al. Stretch-induced  $ca^{2+}$  independent atp release in hippocampal astrocytes. *The Journal of Physiology*, 596(10):1931–1947, 2018.
- [180] Yidan Xue, Theodosia Georgakopoulou, Anne-Eva Van der Wijk, Tamás I Józsa, Ed van Bavel, and Stephen J Payne. Quantification of hypoxic regions distant from occlusions in cerebral penetrating arteriole trees. *PLoS computational biology*, 18(8):e1010166, 2022.
- [181] Jin Yang, John W Clark, Robert M Bryan, and Claudia S Robertson. Mathematical modeling of the nitric oxide/cgmp pathway in the vascular smooth muscle cell. *American Journal of Physiology-Heart and Circulatory Physiology*, 289(2):H886–H897, 2005.
- [182] Joshua J Zaritsky, Delrae M Eckman, George C Wellman, Mark T Nelson, and Thomas L Schwarz. Targeted disruption of *kir2.1* and *kir2.2* genes reveals the essential role of the inwardly rectifying  $k^{+}$  current in  $k^{+}$ -mediated vasodilation. *Circulation research*, 87(2):160–166, 2000.
- [183] Karl Zilles and Bernhard Tillmann. *Anatomie*. Springer-Verlag, 2011.
- [184] Berislav V Zlokovic. The blood-brain barrier in health and chronic neurodegenerative disorders. *Neuron*, 57(2):178–201, 2008.